SUOMEN GEODEETTISEN LAITOKSEN JULKAISUJA
VERÖFFENTLICHUNGEN DES FINNISCHEN GEODÄTISCHEN INSTITUTES
PUBLICATIONS OF THE FINNISH GEODETIC INSTITUTE

N:o 146

EMPIRICAL STUDIES ON MULTIANGULAR, HYPERSPECTRAL, AND POLARIMETRIC REFLECTANCE OF NATURAL SURFACES

by

Juha Suomalainen

Academic dissertation in Physics

To be presented, with the permission of the Faculty of Science of the University of Helsinki, for public criticism in the Auditorium XII of the Main Building (Unioninkatu 34) on 21th of September, 2012, at 12 o'clock noon.

KIRKKONUMMI 2012

Supervisors:
Jouni Peltoniemi
Finnish Geodetic Institute, Finland

Sanna Kaasalainen
Finnish Geodetic Institute, Finland

Pre-examiners:
Andres Kuusk
Tartu Observatory, Estonia

Kai Peiponen
University of Eastern Finland, Finland

Opponent:
Michael K. Shepard
Bloomsburg University, Pennsylvania, USA

Custos:
Karri Muinonen
University of Helsinki, Finland

ISBN (printed): 978-951-711-290-1
ISBN (pdf): 978-951-711-291-8
ISSN: 0085-6932

Juvenes Print – Tampereen Yliopistopaino Oy
Tampere 2012

Abstract

The reflectance factor is a quantity describing the efficiency of a surface to reflect light and affecting the observed brightness of reflected light. It is a complex property that varies with the view and illumination geometries as well as the wavelength and polarization of the light. The reflectance factor response is a peculiar property of each target surface. In optical remote sensing, the observed reflectance properties of natural surfaces are used directly for, e.g., classifying targets. Also, it is possible to extract target physical properties from observations, but generally this requires an understanding and modeling of the reflectance properties of the target. The most direct way to expand our understanding of the reflectance properties of natural surfaces is through empirical measurements.

This thesis presents three original measurement setups for obtaining the reflectance properties of natural surfaces and some of the results acquired using them. The first instrument is the *Finnish Geodetic Institute Field Goniospectrometer* (FIGIFIGO); an instrument for measuring the view angle dependency of polarized hyperspectral reflectance factor on small targets. The second instrument is an unmanned aerial vehicle (UAV) setup with a consumer camera used for taking measurements. The procedure allows 2D-mapping of the reflectance factor view angle dependency over larger areas. The third instrument is a virtual hyperspectral LiDAR, i.e. a setup for acquiring laser scanner point clouds with 3D-referenced reflectance spectra ([$x,y,z,R(\lambda)$]).

During the research period 2005–2011, the FIGIFIGO was used to measure the angular reflectance properties of nearly 400 remote sensing targets, making the acquired reflectance library one of the largest of its kind in the world. These data have been exploited in a number of studies, including studies dealing with the vicarious calibration of airborne remote sensing sensors and satellite imagery and the development and characterization of reflectance reference targets for airborne remote sensing sensors, and the reflectance measurements have been published as a means of increasing the general understanding of the scattering of selected targets. The two latter instrument prototypes demonstrate emerging technologies that are being used in a novel way in remote sensing. Both measurement concepts have shown promising results, indicating that, in some cases, it can be beneficial to use such a methodology in place of the traditional remote sensing methods. Thus, the author believes that such measurement concepts will be used more widely in the near future.

Keywords: Reflectance factor, Multiangular, Polarization, Hyperspectral, Goniospectrometer, Unmanned aerial vehicle, LiDAR

Tiivistelmä

Heijastuskerroin on kullekin kohteelle yksilöllinen ominaisuus joka kuvaa kohteesta heijastuneen valon määrää. Heijastuskertoimen arvo riippuu havainto- ja valaistusgeometriasta sekä valon aallonpituudesta ja polarisaatiosta. Useimmissa optisen kaukokartoituksen menetelmissä mitataan kohteiden heijastuskerrointa. Näitä heijastuskerroinhavaintoja käytetään suoraan esim. kohteiden luokittelussa. Kehittyneemmissä menetelmissä havainnoista on myös mahdollista irrottaa joitain kohteen fysikaalisia ominaisuuksia, mutta yleensä tämä edellyttää kohteen ymmärtämistä sekä valonsironnan mallintamista. Suorin tapa laajentaa ymmärrystä luonnon pintojen valonsironnasta on tehdä empiirisiä mittauksia.

Tässä väitöskirjassa esitellään kolme mittalaitetta luonnon pintojen valonsironnan mittaamiseksi sekä näillä laitteilla kerättyjä tuloksia. Ensimmäinen esiteltävä mittalaite on *Finnish Geodetic Institute Field Goniospectrometer* (FIGIFIGO), jolla voidaan mitata kohteen sirottaman valon suuntariippuvuutta valon aallonpituuden sekä polarisaation funktiona. Toinen mittalaite on automaattinen miehittämätön helikopteri. Kopteriin asennetun kameran sekä kuvien yhdistämismenetelmän avulla maaston valonsironnan suuntariippuvuutta voidaan kartoittaa laajemmilla alueilla kuin FIGIFIGO:a käyttäen. Kolmas mittalaite on virtuaalinen valkean valon LiDAR, jolla voidaan mitata laboratoriokohteen 3D rakenne yhdessä heijastusspektrien kanssa ([x,y,z,R(λ)]).

Tutkimusjakson (2005–2011) aikana FIGIFIGO:a on käytetty lähes 400 kaukokartoituskohteen sironnan suuntariippuvuuden mittaamiseen. Näillä mittauksilla kerätty datakirjasto on yksi maailman suurimmista ja kattavimmistaan lajissaan. FIGIFIGO-mittauksia on hyödynnetty useissa tutkimuksissa esim. satelliitti havaintojen ja kaukokartoitus sensoreiden lennonaikaisessa kalibroinnissa ja validoinnissa, sekä ilmakuvauksen heijastuskerroinreferenssikohteiden kehittämisessä. Mittaustulokset on myös julkaistu tieteellisissä julkaisuissa laajentaen yleistä ymmärrystä kaukokartoituskohteiden valonsironnasta. Kaksi jälkimmäistä mittalaitetta ovat prototyyppejä joilla on testattu ja demonstroitu uutta tekniikkaa jota ei ole aiemmin hyödynnetty kaukokartoituksessa tällä tavoin. Molemmat mittauskonseptit tuottivat lupaavia tuloksia mahdollistaen uudentyyppisten mittausten tekemisen. Saadut tulokset antavat ymmärtää että mittauskonseptien kehittämistä kannattaa jatkaa ja on todennäköistä että tämän kaltaiset mittausmenetelmät tulevat jo lähitulevaisuudessa leviämään laajempaan käyttöön kaukokartoituksessa.

Avainsanat: Heijastuskerroin, Suuntariippuvuus, Polarisaatio, Spektri, Goniometri, UAV, LiDAR

Preface

In spring 2004, I was a third-year physics student at the University of Helsinki when I saw a job announcement for a position as a research assistant in the Department of Remote Sensing and Photogrammetry in the Finnish Geodetic Institute (FGI). I needed a summer job and possibly also a topic for my master's thesis, so I decided to apply for the position. At the time, I knew nothing about remote sensing and, to be frank, I do not think that I had ever even heard the word geodesy. I was selected for the position and it turned out that the position was more about developing and using measurement systems for the retrieval of reflectance factors than traditional geodesy. I found the topic of remote sensing applications presented by the research group to be interesting. In 2006, I received my master's degree in physics; my thesis, titled "Multiangular Spectrometry and Optical Properties of Debris Covered Surfaces," was based on the research work done at the FGI. Since completing the master's degree, I have continued as a PhD student doing research at the FGI.

The research that I have done at the FGI has allowed me to learn about various aspects of empirical research on optical remote sensing. I have led or taken part in the construction of a number of optical measurement systems; the three major measurement systems are presented in this thesis. I have made a major personal contribution during all phases of development, including defining the measurement problem, constructing the setup, calibrating the system, programming the data processing algorithms, analyzing the data, and, finally, publishing the results. I have also had the privilege to learn about the reflectance properties of natural surfaces and emerging remote-sensing technologies, including automated unmanned aerial vehicles and supercontinuum laser sources.

I would like to thank all my co-authors in the publications and my colleagues at the FGI for their co-operation and help in the research. I would especially like to thank Dr. Jouni Peltoniemi and Dr. Sanna Kaasalainen for their continuous assistance and guidance throughout my whole research career. I also want to express my sincere gratitude to my family and friends for their support.

Kirkkonummi, September 2012

Juha Suomalainen

Department of Remote Sensing and Photogrammetry
Finnish Geodetic Institute
P.O.Box 15, Geodeetinrinne 2, 02431, Masala, Finland

Contents

Table of contents for the summary part of the thesis.

Original publications

The dissertation is based on the following scientific publications, referred to in the text by their Roman numerals:

I **Juha Suomalainen**, Teemu Hakala, Jouni Peltoniemi, and Eetu Puttonen (2009) *Polarised Multiangular Reflectance Measurements Using the Finnish Geodetic Institute Field Goniospectrometer.* Sensors 9, 3891-3907; doi: 10.3390/s90503891

II **Juha Suomalainen**, Teemu Hakala, Eetu Puttonen, and Jouni Peltoniemi (2009). *Polarised Bidirectional Reflectance Factor Measurements from Vegetated Land Surfaces.* Journal of Quantitative Spectroscopy & Radiative Transfer 110, 1044–1056; doi: 10.1016/ j.jqsrt.2009.02.017

III Jouni Peltoniemi, Teemu Hakala, **Juha Suomalainen**, and Eetu Puttonen (2009) *Polarised Bidirectional Reflectance Factor Measurements from Soil, Stones, and Snow*. Journal of Quantitative Spectroscopy & Radiative Transfer 110, 1940–1953; doi: 10.1016/ j.jqsrt.2009.04.008

IV Eetu Puttonen, **Juha Suomalainen**, Teemu Hakala, and Jouni Peltoniemi (2009). *Measurement of Reflectance Properties of Asphalt Surfaces and Their Usability as Reference Targets for Aerial Photos*. IEEE Transactions on Geoscience and Remote Sensing 47(7), 2330–2339; doi: 10.1109/ TGRS.2008.2010132

V Teemu Hakala, **Juha Suomalainen,** and Jouni Peltoniemi (2010) *Acquisition of Bidirectional Reflectance Factor Dataset Using a Micro Unmanned Aerial Vehicle and a Consumer Camera*. Remote Sensing 2, 819-832; doi:10.3390/rs2030819

VI **Juha Suomalainen**, Teemu Hakala, Harri Kaartinen, Esa Räikkönen, and Sanna Kaasalainen (2011) *Demonstration of a Virtual Active Hyperspectral LiDAR in Automated Point Cloud Classification*. ISPRS Journal of Photogrammetry and Remote Sensing 66, 637–641; doi: 10.1016/ j.isprsjprs.2011.04.002

VII Eetu Puttonen, **Juha Suomalainen**, Teemu Hakala, Esa Räikkönen, Harri Kaartinen, Sanna Kaasalainen, and Paula Litkey (2010) *Tree Species Classification from Fused Active Hyperspectral Reflectance and LiDAR Measurements*. Forest Ecology and Management 260, 1843–1852; doi: 10.1016/ j.foreco.2010.08.031

Author's contribution

This dissertation consists of an introductory part and seven scientific publications. The introductory part presents the research problem and goals, gives an overview of related research, describes the research methods, summarizes the results, and provides a discussion and draws conclusions about the findings from each of the publications. The publications themselves provide more detail on these issues.

The first publication (***I***) introduces the *Finnish Geodetic Institute Field Goniospectrometer* (FIGIFIGO), describes the measurement procedure, analyzes the error propagation in measurements, and presents some sample data. The author has been responsible for developing the instrumentation, the measurement procedure, and the whole data processing chain, and has written most of the paper. The co-authors have helped develop the instrument and take the measurements.

The three next publications (***II***–***IV***) present the polarized bidirectional reflectance factors of selected targets measured using the FIGIFIGO. The author has led or taken part in the measurements, pre-processed most of the datasets, taken part in analyzing and interpreting the data, and helped write the papers.

The fifth publication (***V***) presents a system that uses a camera mounted on an unmanned aerial vehicle (UAV) to measure the land-surface, hemispherical-directional reflectance factor and compares the results with the ground truth acquired using the FIGIFIGO. The author developed the measurement method and the data processing chain in co-operation with Teemu Hakala. The measurements were taken by all of the authors working in co-operation. Teemu Hakala performed the data processing and wrote most the paper.

The sixth publication (***VI)*** presents a demonstration of a virtual hyperspectral LiDAR system and evaluates the performance of hyperspectral point cloud classification methods. The author developed the system in co-operation with Teemu Hakala, Esa Räikkönen, and Sanna Kaasalainen. Harri Kaartinen provided the monochromatic LiDAR data. The author developed and performed all data processing and wrote most of the paper.

The seventh publication (***VII***) evaluates the performance of the hyperspectral LiDAR dataset in tree species classification using data collected with the system presented in publication **VI**. The author took part in the measurements and assisted in processing and analyzing the data.

List of abbreviations

BRDF	Bidirectional Reflectance Distribution Function
BRF	Bidirectional Reflectance Factor
FGI	Finnish Geodetic Institute
FIGIFIGO	Finnish Geodetic Institute Field Goniospectrometer
HDRF	Hemispherical-Directional Reflectance Factor
HSS	Hyperspectral Scanner
LiDAR	Light Detection and Ranging
RPV model	Rahman-Pinty-Verstraete model
SCM	Spectral Correlation Mapper
TLS	Terrestrial Laser Scanner
UAV	Unmanned Aerial Vehicle

List of symbols

Quantity	**Symbol**	**Unit**
Radiance	L	$[\mathrm{W/m^2/sr/nm}]$
Irradiance	E	$[\mathrm{W/m^2/nm}]$
Reflectance factor	R	[1]
Wavelength of light	λ	[nm]
Zenith angle of incident illumination	θ_i	[°]
Azimuth angle of incident illumination	φ_i	[°]
Zenith angle of reflectance	θ_r	[°]
Azimuth angle of reflectance	φ_r	[°]
Incident	$_i$	
Reflected	$_r$	
Ideal (lossless and Lambertian)	$_{id}$	
Stokes vector (radiances)	$\mathbf{S}$	$[\mathrm{W/m^2/sr/nm}]$
Mueller matrix	$\mathbf{M}$	[1]
Mueller matrix component	m_{ij}	[1]

1. Introduction

Fig. 1. A panorama picture taken just before the sunset during the 2006 measurement campaign in Abisko, Sweden. A number of light-scattering effects can be seen. A thin rain above the lake produces a beautiful rainbow. Across the valley and next to the shadow of the mountain, the hot-spot effect brightens the reflectance from the forest in a direct backscattering direction. A view-angle effect can be seen in how the proportional area of visible shadows on the ground changes between the backscattering direction and the side angles. If only the intensity is considered, the lake is more or less evenly illuminated. However, the reflecting surface and the position of the clouds in the forward direction causes variations in the observed brightness.

Reflectance from the surfaces surrounding us is a more complex issue than one would immediately assume. The reflected light that we observe is not just defined by the simple terms like general color and brightness of the surface, but is also affected by the light-scattering properties of the surface and the view angle, as well as by the brightness, color, and angular distribution of the illumination – just to name a few. The human brain analyzes the observations and, despite all the variations, is able to identify targets with superb accuracy. In optical remote sensing, cameras and other sensors basically collect the same data as our eyes do and the math used in automation should perform a similar analysis as our brains do.

In remote sensing, the questions that need to be solved via observations are often quite statistical in nature, such as “Should this hectare be classified as a mixed forest or as a pure conifer forest?” or “Should we add fertilizer to this wheat field?” Answering such questions always requires some sort of modeling of the target. In simple cases, the models can be empirical linear regressions, for example between the vitality of the vegetation and the color of the reflected light, while the other extreme involves a 50-parameter physical model of the forest’s reflectance.

A common approach to analyzing optical data is to study the brightness and color of the observation. Most remote sensing instruments measure the intensity (=radiance) of the reflected light. Sometimes the radiances are used to directly compare the intensities within the dataset, but most often the radiances

are converted to reflectance factors. The reflectance factor is a quantity describing the brightness of a target (Schaepman-Strub, et al. 2006). To describe it plainly, the reflectance factor is 0 for a black target and 1 for a matte white target. To convert the radiance observations to reflectances, a calibration is required. For the calibration, additional information is needed: either the brightness (=irradiance) of the illumination or a measurement of a reflectance reference target within the dataset. The former is used most commonly for the operational calibration of a satellite or aerial images and the latter for local, ground-based measurements.

In remote sensing, the reflectance factor observations make it possible to extract the physical properties of the target. A number of spectral indices have been found that correlate with the structure and chemical composition of the vegetated and inorganic targets (Sims and Gamon, 2002). The reflectance factor response is a result of the reflections and absorptions of light occurring within the target. These reflectance processes are also directly linked to the radiative energy balance of the surface, which is realized, e.g., as the melting speed of the snow (Yang, et al., 2001), or as the efficiency of the vegetation at photosynthetically exploiting light (Verstraete, et al., 2008). These processes are quantities that are directly significant for climate and environmental studies. As a more indirect application, reflectance factor observations can be compared with the reference data from data libraries or with reflectance models, which allows for target classification and the extraction of physical properties.

Each sample of natural targets has a peculiar spectrum and angular distribution of reflectance. Theoretical and empirical models can be used to simulate reflectances for a wide range of targets, such as leaves (Feret, et al., 2008), forests (Widlowski, et al., 2006), general vegetation (Jacquemoud, et al., 2009), and soil (Taixia and Yunsheng, 2005). However, because the natural targets are generally extremely complex to describe and parameterize, the only way to reliably retrieve the reflectance properties of a particulate sample is via measurements.

This dissertation is based on empirical studies exploiting three novel instruments developed for retrieving the reflectance factor data of natural surfaces. The motivation for developing these new instruments can be attributed to three equally important topics. The first motivation merely had to do with plain curiosity about scattering physics. Light scattering on natural surfaces is still not properly understood and the only way to expand our understanding of it is via measurements. The second motivation was to develop new remote sensing concepts using emerging technologies. The third one was a practical one; to provide reference data for evaluating reflectance models and practical remote sensing research applications.

Chapter 2 of the dissertation presents the key theories and mathematical methods behind reflectance factor retrieval. The three measurement instruments used in the studies are presented briefly in chapter 3. The acquired reflectance data are reviewed in chapter 4. Finally, chapter 5 provides conclusions about the retrieved results and presents an outlook for future research and applications.

2. Theory

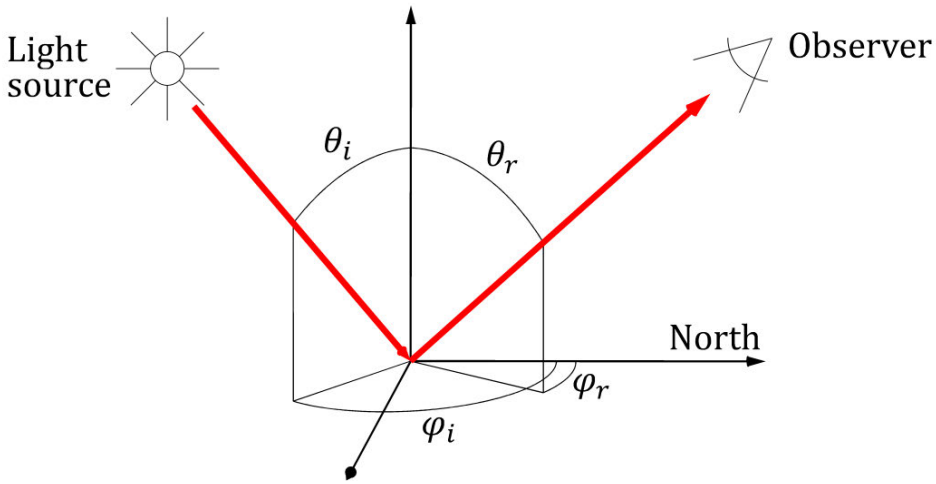

Fig. 2. The bidirectional reflectance geometry defined using the zenith (θ) and azimuth (φ) angles of incidence and reflectance.

Figure 2 shows a typical geometry for an optical observation of a target. A target is illuminated by a light source in a single direction or by a hemispherical distribution of incident light. The reflectance properties of the target define the amount and type of light that if scattered towards the observer. These reflectance properties are most commonly described using a quantity called the reflectance factor. The reflectance factor is defined as follows (Schaepman-Strub, et al., 2006):

$$R(\theta_i, \varphi_i, \theta_r, \varphi_r) = \frac{L(\theta_i, \varphi_i, \theta_r, \varphi_r)}{L_{id}(\theta_i, \varphi_i, \theta_r, \varphi_r)} \quad (1.)$$

where L and L_{id} are, respectively, the radiances [W/m^2/sr] reflected from a target and an ideal (lossless and Lambertian) reference panel measured in the same reflectance geometry (θ_i, φ_i, θ_r, φ_r). The azimuth and zenith angles of the geometry are defined in Fig. 2. The radiometric quantities (*L, E, R*) are always functions of the wavelength of light; it should always be assumed that the quantities used when calculating the reflectance factor employ an identical spectral band. The wavelength dependencies *(..., λ)* have been omitted from the equations for the sake of simplicity.

Unfortunately, ideal reference panels, such as those required by Equation 1, are not available. Thus, there are two practical methods for producing reflectance factors: A method exploiting a reference panel with a known reflectance factor (Equation 2) and one exploiting the incident irradiance acquired from a measurement or an atmospheric model (Equation 3). The equations for producing such reflectance factors are as follows:

$$R(\theta_i, \varphi_i, \theta_r, \varphi_r) = \frac{L(\theta_i, \varphi_i, \theta_r, \varphi_r)}{L_{ref}(\theta_i, \varphi_i, \theta_r', \varphi_r')} R_{ref}(\theta_i, \varphi_i, \theta_r', \varphi_r') \quad (2.)$$

$$R(\theta_i, \varphi_i, \theta_r, \varphi_r) = \pi \frac{L(\theta_i, \varphi_i, \theta_r, \varphi_r)}{E_i(\theta_i, \varphi_i)} \quad (3.)$$

The reference panel method is commonly used in field measurements because it is simple to use and requires only a single instrument in stable illumination conditions. When using this method, an absolute radiometric calibration is not needed, because the only requirement is a linear response to radiance. The incident irradiance method is commonly used in satellite and airborne applications to calibrate images without any ground reference. A drawback is that the accuracy of this method depends directly on the radiometric calibration quality of the instrumentation and atmospheric correction.

The reflectance factor is always a function of both illumination and reflectance geometry. The reflectance factor is referred as *Bidirectional Reflectance Factor* (BRF) if both the illumination and view directions are directional, as shown in Fig. 2. When strictly applying the definition, the bidirectional geometry cannot exist as a measureable quantity because measurements are always taken using a finite sensor with a conical field-of-view. However, because the natural surfaces tend to have a rather smooth angular dependency of BRF outside the direction of direct backscatter (**I**–**IV**), narrow conical field-of-views can be ignored and the direction approximated. Most remote sensing observations and all of the measurements presented in this dissertation were taken using optics with smaller than 5° opening angle and, thus, the reflectance factors produced can be referred to as having a directional view geometry as well as a conical one. In laboratory measurements where collimated light is used for illumination, the condition for bidirectional geometry is satisfied and, thus, the reflectance factors can be referred to as BRF. In natural sunlight illumination, there is always a hemispherical component present in the illumination. The reflectance factors obtained in such conditions are referred to as *Hemispherical-Directional Reflectance Factor*s (HDRF) or, to be more precise, as *field-HDRF*s to highlight the anisotropy of the diffuse component. If the diffuse component is also measured, it is possible to acquire the BRF in natural sunlight conditions. The theory and equations for this are presented in publication **I**.

The angle dependency and the general level of the reflectance factor are produced by a number of scattering processes related to the properties of the target. The scattering processes can usually be distributed to single- and multiple-scattering effects. In single scattering, incident light enters the target and scatters directly outwards. Single-scattering processes usually produce BRFs with distinct effects and high anisotropy; these are produced by, e.g., specular reflections on shiny surfaces. The anisotropy of single scattering is also affected in an exaggerated manner by the self-shadowing of the target, which commonly produces some relative brightening in the backward direction. In multiple scattering, incident light scatters back and forth inside the target medium before exiting it. BRFs from multiple-scattering processes are usually more isotropic than those from single-scattering processes, but their intensities are affected in an exaggerated manner by the absorptions occurring in the reflections and transmittances. Thus, multiple scattering is usually a leading scattering mechanism for targets and wavelengths with a high reflectance factor, while darker ones usually emphasize more single-scattering processes.

In the direct backscattering direction and a few degrees around it, a strong brightening occurs (see Fig. 1), which is known in remote sensing as the hot-spot effect and in astronomy as the opposition surge or

Seeliger effect. The hot-spot effect is caused by two phenomena: Shadow hiding and coherent backscattering (Hapke, 1993). Shadow hiding is simply caused by the fact that in the direct backscattering direction, an observer does not have any shadows in her or his line of sight, resulting in an observation of bright intensity. Coherent backscatter is caused by a more complex process known in optics as a weak localization of photons (Wiersma, et al., 1997, Strangi, et al., 2006), where the multiple-scattering paths present in the medium are utilized by light components travelling both directions. In the direct backscattering direction, these components travel exactly the same optical path and are combined coherently, producing up to a two-fold increase in the reflected intensity. In a remote sensing context, the hot spot in particular increases the intensities received by Light Detection and Ranging (LiDAR) systems, which always observe the target from the direct backscattering direction. The hot-spot effect can also often be detected from airborne or satellite-based imagery. With ground-level measurements, the hot spot is usually undetectable because the brightening is hidden by the shadow from the sensor optics or by the viewer's head.

The polarization of light is a quantity describing the orientation of the electromagnetic wave oscillation. The polarization state of light is often described using Stokes parameters, which are combined as a Stokes vector (***S***) (Tyo, et al., 2006):

$$\boldsymbol{S} = \begin{bmatrix} I \\ Q \\ U \\ V \end{bmatrix} \propto \begin{bmatrix} L_{0^\circ} + L_{90^\circ} \\ L_{0^\circ} - L_{90^\circ} \\ L_{45^\circ} - L_{135^\circ} \\ L_{left} - L_{right} \end{bmatrix} \tag{4.}$$

where I represents the parameter for intensity, Q and U represent the linear polarization, and V represents the circular polarization. The values L_{N° represent the radiances received by a sensor equipped with a linear polarization filter in orientation $N°$. L_{left} and L_{right} are similar radiances collected using a circular polarization filter. The effect of an optical component or a reflecting surface on a Stokes vector of light passing through it is expressed using the Mueller matrix (***M***) calculus:

$$\boldsymbol{S}_r = \boldsymbol{M}\boldsymbol{S}_i = \begin{bmatrix} m_{00} & m_{01} & m_{02} & m_{03} \\ m_{10} & m_{11} & m_{12} & m_{13} \\ m_{20} & m_{21} & m_{22} & m_{23} \\ m_{30} & m_{31} & m_{32} & m_{33} \end{bmatrix} \begin{bmatrix} I_i \\ Q_i \\ U_i \\ V_i \end{bmatrix} \tag{5.}$$

where $\boldsymbol{S}_i$ and $\boldsymbol{S}_r$ are the Stokes vectors of incident and reflected light and m_{ij} are the Mueller matrix components. In this notation, we can see that the component m_{00} is the same as the reflectance factor defined in Equations 1–3. The Mueller matrix calculus can also be used to describe the reflectance in bidirectional geometry from a natural surface using the following equation:

$$\boldsymbol{S}_r(\theta_r, \varphi_r) = \boldsymbol{M}(\theta_i, \varphi_i, \theta_r, \varphi_r)\boldsymbol{S}_i(\theta_i, \varphi_i) \tag{6.}$$

In passive remote sensing, the incident illumination is usually sunlight. The diffuse, blue sky component of sunlight is polarized because it is formed almost purely by Rayleigh scattering (Pust, et al., 2011), but the direct component has only negligible polarization. Thus, the incident Stokes parameters Q, U, and V are practically zero, because the polarization that occurs as part of the diffuse blue sky component of sunlight is mixed with the hemisphere of the incident angles. Natural targets also produce little circular polarization (Sparks, et al., 2009) relative to linear polarization and, thus, the

Mueller component m_{30} can be assumed to be zero for most applications. With these approximations, the Stokes vector for reflected light can be written as follows:

$$\boldsymbol{S}_r(\theta_i, \varphi_i, \theta_r, \varphi_r) = \begin{bmatrix} m_{00}(\theta_i, \varphi_i, \theta_r, \varphi_r) \\ m_{10}(\theta_i, \varphi_i, \theta_r, \varphi_r) \\ m_{20}(\theta_i, \varphi_i, \theta_r, \varphi_r) \\ 0 \end{bmatrix} I_i \tag{7.}$$

The remaining Mueller matrix components can be determined if the Stokes vector of reflected light is measured using a linear polarization filter. By replacing the Stokes vector parameters in Equation 7 with the radiance notation from Equation 4, the retrieval functions for the Mueller components using a linearly polarized sensor and a reference panel can be written as follows:

$$R(\theta_i, \varphi_i, \theta_r, \varphi_r) = m_{00}(\theta_i, \varphi_i, \theta_r, \varphi_r) = \frac{L_{0°}(\theta_i, \varphi_i, \theta_r, \varphi_r) + L_{90°}(\theta_i, \varphi_i, \theta_r, \varphi_r)}{L_{ref,0°}(\theta_i, \varphi_i, \theta_r', \varphi_r') + L_{ref,90°}(\theta_i, \varphi_i, \theta_r', \varphi_r')} R_{ref}(\theta_i, \varphi_i, \theta_r', \varphi_r') \tag{8.}$$

$$m_{10}(\theta_i, \varphi_i, \theta_r, \varphi_r) = \frac{L_{0°}(\theta_i, \varphi_i, \theta_r, \varphi_r) - L_{90°}(\theta_i, \varphi_i, \theta_r, \varphi_r)}{L_{ref,0°}(\theta_i, \varphi_i, \theta_r', \varphi_r') + L_{ref,90°}(\theta_i, \varphi_i, \theta_r', \varphi_r')} R_{ref}(\theta_i, \varphi_i, \theta_r', \varphi_r') \tag{9.}$$

$$m_{20}(\theta_i, \varphi_i, \theta_r, \varphi_r) = \frac{L_{45°}(\theta_i, \varphi_i, \theta_r, \varphi_r) - L_{135°}(\theta_i, \varphi_i, \theta_r, \varphi_r)}{L_{ref,0°}(\theta_i, \varphi_i, \theta_r', \varphi_r') + L_{ref,90°}(\theta_i, \varphi_i, \theta_r', \varphi_r')} R_{ref}(\theta_i, \varphi_i, \theta_r', \varphi_r') \tag{10.}$$

The linear polarization components m_{10} and m_{20} of the Mueller matrix are often converted into a single, more convenient value of Degree of Linear Polarization (DOLP), which describes the polarization of the reflected light:

$$\text{DOLP} = \frac{\sqrt{Q^2 + U^2}}{I} = \frac{\sqrt{{m_{10}}^2 + {m_{20}}^2}}{m_{00}} \tag{11.}$$

Especially for measurements taken on a principal scattering plane, it is common that most of the polarization is in the m_{10} component, which describes the balance of horizontal and vertical polarization. Thus, it is a common practice to visualize the results as a "–Q/I"-ratio that can be calculated as a ratio of "$-m_{10}/m_{00}$". If the Stokes U component equals zero, the "–Q/I"-ratio values give similar values as the DOLP, with the exception that its values range from -1 to +1, indicating also the horizontal-vertical balance of the polarization. As a result, this particular ratio is sometimes also called the degree of polarization.

3. Instruments

The work presented in this dissertation is based on measurements collected using three instruments briefly presented in this chapter. The descriptions, with more technical details, can be found in publications **I**, **V**, and **VI.**

Finnish Geodetic Institute Field Goniospectrometer (FIGIFIGO)

In remote sensing, the accurate reflectance factor of a target is often needed for various reasons; for example, aerial photography campaigns often exploit a large reflectance reference surface on the ground for vicarious calibration or validation of the produced reflectance factor images. The reflectance factors of such surfaces are often determined using a simple handheld spectrometer, but for more accurate results the view angle must also be taken into account. A field-capable goniospectrometer that measures the BRF/HDRF is needed for this.

A goniospectrometer is a device that measures the reflectance factor of a target from multiple viewing angles. One of the first well-known instruments was built at the European Goniometer Facility (EGO) (Koechler, et al., 1994). The EGO is a laboratory system that rotates the spectrometer in a hemisphere around the sample at approximately a 2-meter radius, and, in this way, measures the reflected radiance from selected viewing angles. To gain an adequate sampling of the BRF, the measurements are repeated at multiple illumination zenith angles. Although there are many advantages to measuring the BRF in a laboratory, in some cases in-situ measurements are required, e.g. if the measurements need to be taken at the same time as airborne observations or if the samples cannot be moved to a laboratory. Also, differences in laboratory illumination and sunlight make it challenging to directly compare field data with the laboratory results.

To address the need for in-situ measurements, a number of field goniospectrometers for measuring a single, selected target have been built. The field goniometers can basically be divided into two classes: Inbound observing goniometers, which measure small targets in the center of the goniometer, and outbound observing goniometers, which measure the properties of large homogeneous landscapes. In this paragraph, only the inbound observing field goniometers are reviewed. FIGOS (Schopfer, et al., 2008), the Sandmeier Field Goniometer (Turner, 1998), and the previous version of the Finnish Geodetic Institute's goniometer (Peltoniemi, et al., 2005) are almost direct descendants of the EGO design. Although these instruments have been adapted to field operations, they are heavy for manual transportation. The IAC ETH Goniospectrometer by the Institute for Atmospheric and Climate Science of the Swiss Federal Institute of Technology presented a novel boom-mounted goniospectrometer designed for measuring snowy surfaces (Bourgeois, et al., 2006). Measurements taken using a similar instrument have also been published by Kokhanovsky et al. (2005). Pegrum et al. have presented the GRASS system, which has an interesting design that exploits multiple fiber-optic light collectors and no moving parts (Pegrum, et al., 2006). Also, smaller field goniometers that use the traditional inbound measurement principle have been built, e.g. the automated spectro-goniometer (Painter, et al., 2003), the University of Lethbridge Goniometer System (Coburn and Peddle, 2006), the Compact Laboratory Spectro-Goniometer (CLabSpeG) (Biliouris, et al., 2007), and unnamed instruments by the university of Hamburg (Meister, et al., 1996), the Italian National Research Council (CNR-IREA) (Giardino and Brivio, 2003), and the University of Alaska Fairbanks (Li and Zhou, 2004). The smaller instruments have increased mobility, but as a drawback the short viewing distance limits the size of the sample area.

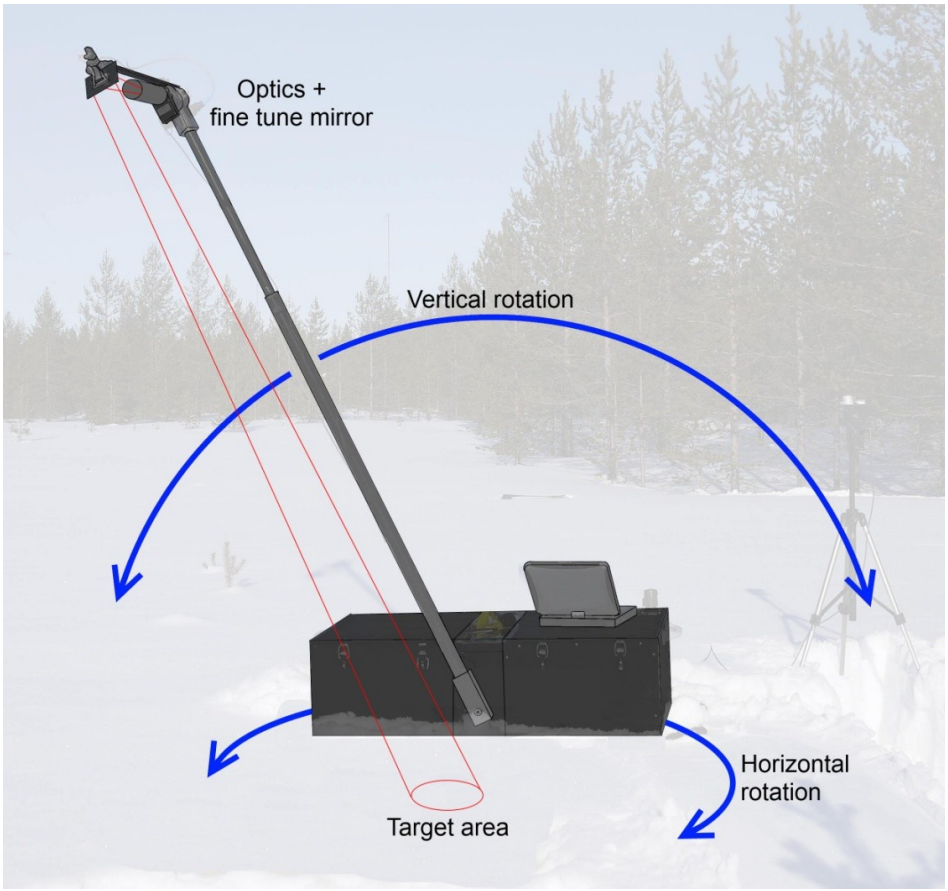

Fig. 3. An augmented photograph of the FIGIFIGO in operation. The radiance reflected from the target is measured with the optics at the top of the arm. An optical fiber runs down from the optics to a spectrometer placed inside the goniometer casing. With the single push of a button, a motor rotates the arm from side to side, collecting an array of radiance measurements. A full hemisphere of radiances is acquired by manually rotating the FIGIFIGO around the target and repeating the vertical procedure. The radiances are converted into reflectance factors by normalizing them with the reference panel measurements and by applying a number of calibrations.

Having a large sample size is advantageous, especially when heterogeneous samples are measured, because the sample size improves the representativeness of the sample. Sample heterogeneity is a significant problem, especially with natural vegetation samples (Milton, et al., 2009).

The *Finnish Geodetic Institute Field Goniospectrometer* (FIGIFIGO, see Fig. 3 and publication **I**) has been designed from the start as a portable device for measuring natural heterogeneous samples. The FIGIFIGO has a similar measurement distance as the large EGO-type goniometers, allowing for samples up to 25 cm in diameter while using 3° optics. Instead of a heavy frame surrounding the target,

the FIGIFIGO operates from one side of the target and uses a single lightweight arm for positioning the sensor optics over and around the target. This principle is made possible by exploiting a spectrometer with an optical fiber, which makes it possible to keep all the heavy instrumentation static at ground level. This principle makes the goniometer very compact and lightweight and it minimizes the self-shadowing effect. The FIGIFIGO has a high level of automation when data is being collected , which makes it trouble free and reliable to use when in the field. Other advanced features of the FIGIFIGO include:

- Inclinometers for determining the view zenith direction independent of the slope of terrain
- Solar compass for determining the goniometer azimuth orientation
- GPS receiver for determining location and providing data for calculating the solar elevation
- Active, fine-tuning mirror in the optics for stabilizing the position of the field-of-view during the zenith movement
- Laser pointers for marking the edges of the field-of-view; these are visible only when spectrometer is not measuring something
- Pyranometer for recording changes in the incident radiant power
- A hemispherical sky camera for automated recording of cloud conditions.

During the processing phase, the raw data from the FIGIFIGO are converted into BRF and HDRF library datasets using detailed Matlab processing algorithms. The collected radiances are normalized for slight variations in incident irradiance using the pyranometer data, and the target radiances are converted into reflectance factors by normalizing them with the reference panel measurements. A diffuse light correction is applied to the HDRF reflectances collected in the field, producing a secondary BRF data product that can be compared directly with the laboratory measurements. A BRF/HDRF dataset is built by coupling the spectra with the instrument's metadata (sensor and illumination angles, location, timing, instrument parameter, etc.) and a number of target description parameters (target name, description, classifications, etc.). The datasets are stored in a standardized file format in a reflectance library.

Optionally, the FIGIFIGO can also be mounted with motorized, linearly polarizing optics. These optics allow the FIGIFIGO to measure linearly polarized reflectance factors (i.e. Mueller matrix components) in a similar fashion as with normal BRFs or HDRFs. Linearly polarized reflectance factors have been measured in laboratory conditions by a number of research groups (Brissaud, et al., 2004; Sun and Zhao, 2011), as well as in field conditions with a limited angular sampling (Leroux, et al., 1998), but to my knowledge the FIGIFIGO is currently the only polarization measuring goniospectrometer in operation that can be used in the field.

Unmanned Aerial Vehicle in HDRF mapping

The FIGIFIGO offered a method for retrieving the HDRF of an individual small target. However, if HDRFs are needed for wider areas, instead of for individual small targets, a method for HDRF mapping is still needed. In an HDRF map, each ground pixel is a dataset containing a number of reflectance factor measurements taken from multiple viewing angles. HDRF maps can be used, e.g., to calculate the albedo, classify land cover, change the level of detection, and extract target properties. Most satellite imaging sensors that are capable of varying the view angle, such as the MODIS (Schaaf, et al., 2002), MISR (Lucht and Lewis, 2000), CHRIS (Barnsley, et al., 2004), and POLDER (Hagolle, et al.,

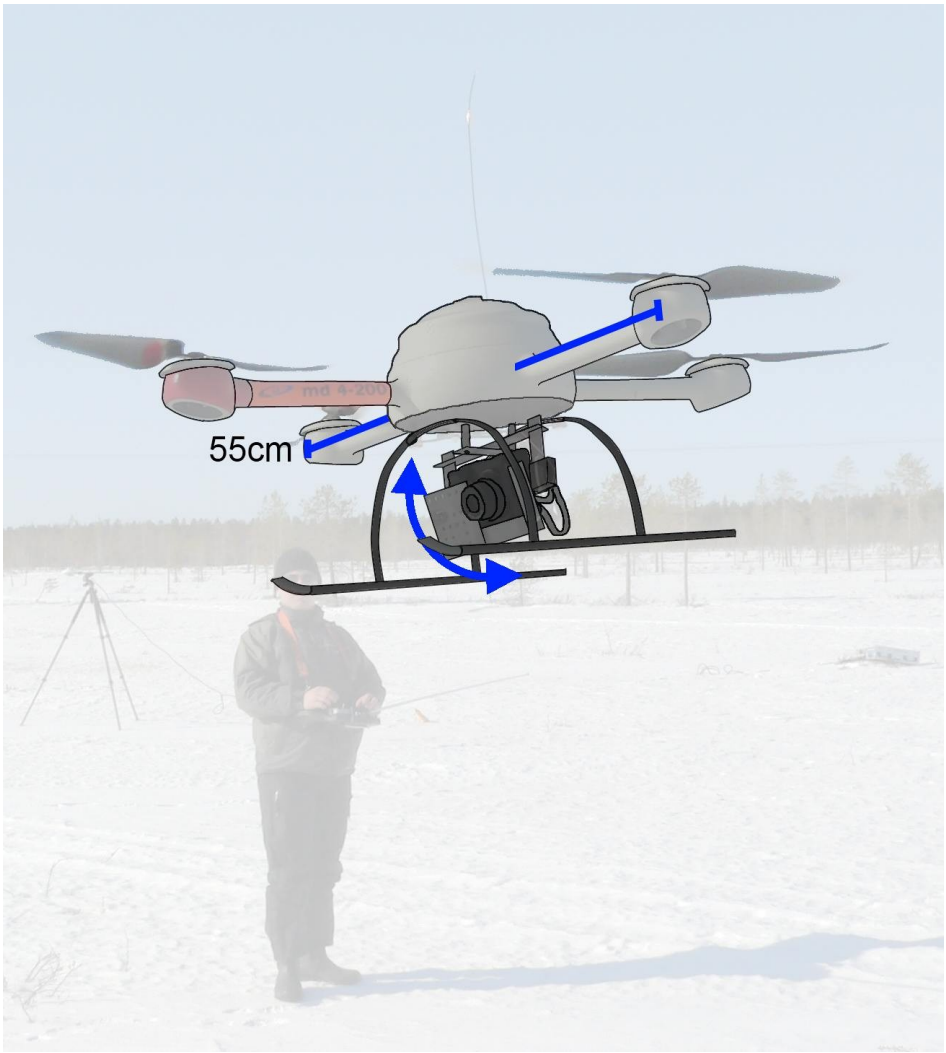

Fig. 4. An augmented photograph of a quadrocopter UAV taking off for a HDRF mapping flight. A consumer digital camera is installed on a tilting camera mount under the UAV. Once airborne, an autopilot maneuvers the UAV through a series of waypoints and camera orientations, taking images of the target area from multiple viewing angles. During the processing phase, the photographs are converted into georeferenced reflectance factor images and fused together, producing a multi-view-angle HDRF map of the area.

1999), are also capable of producing HDRF maps. The satellite sensors can provide global coverage, but their spatial resolution is typically order of tens or hundreds of meters and the hemispherical sets of multiple-view-angle observations are collected over a period of days or weeks. Satellite datasets consisting of multiple observations taken during one overpass can be collected in time scale of minutes, but the view angles in such datasets are limited to a single plane of observations. Airborne observation

systems, such as the Cloud Absorption Radiometer(CAR) (Gatebe, et al., 2003), airborne versions of the POLDER (Auriol, et al., 2008; Leblanc, et al., 1999), the Advanced Solid-state Array Spectroradiometer (ASAS) (Kovalick, et al., 1994), and commercial digital cameras (Ehrlich, et al., 2011), have been used to collect more instantaneous data with a higher spatial resolution.

During the last decade, autonomous Unmanned Aerial Vehicle (UAV) technology has taken a major leap forward. Today, UAVs are an affordable observation platform, filling the gap between manned aircraft-based and ground-based measurements. When compared to traditional aerial remote sensing campaigns using a helicopter or a fixed-wing aircraft, UAV campaigns involve less preliminary planning and offer flexibility in terms of the exact measurement time. Passive optical remote sensing is, in many cases, limited by the weather, and, by using UAVs, an optimal weather gap can be selected for the measurements.

In publication **V**, we presented a novel HDRF mapping concept based on a micro UAV and a consumer camera (Fig. 4.). The UAV used in this study was a MD4-200 quadrocopter by Microdrones GmbH. The MD4-200 can be programmed with a flight plan that defines the points and orientations of the photographs that need to be taken. During the flight, the copter performs the flight plan autonomously, needing pilot interference only during take-off and landing. During the processing phase, the photographs are manually georeferenced using markers on the ground and calibrated with reflectance factor images using a reflectance reference target in the target area. To ensure the necessary radiometric accuracy, it is necessary to apply geometrical and radiometric calibrations for the camera and to take the view-angle effects of the reference target reflectance factor into account. A multi-view-angle HDRF map is produced by fusing the reflectance factor images. See publication **V** for more details on the instrumentation and calibration process.

Virtual Hyperspectral LiDAR

Light Detection and Ranging (LiDAR) is a technique in which the distance of a target is detected. This is done by measuring the time-of-flight for a light pulse traveling forth and back between the instrument and the target. LiDARs are often mounted on a rotating scanner so they can operate in a linear or imaging mode rather than take a single point measurement. These days, such laser scanners are essential in remote sensing. They are commonly used on terrestrial (Lichti, et al., 2008), airborne (Hyyppä, et al., 2009), and satellite missions for 3D mapping of anything from a centimeter scale to a global scale. As more and more 3D data are collected, there is an increasing need for automation in the classification and interpretation of LiDAR data.

In addition to ranging, laser scanners also usually record the intensity of reflected light. Typically, the LiDAR intensities are used in classification to assist with the shape parameters extracted from the 3D data. The monochromatic intensities help in classification, but in many cases even more accurate results could be acquired if multispectral data were available. Dual-wavelength LiDARs are already in use in specific applications; for example, coastal water depths are routinely mapped using green-NIR bathymetric LiDARs (Irish and Lillycrop, 1999), and atmospheric gases are monitored using Differential Absorption LiDARs (Browell, et al., 1998). Since multispectral laser scanners are still rare, a common approach is to fuse monochromatic LiDAR data with other datasets. LiDAR data have successfully been fused with, e.g., photographs (Secord and Zakhor, 2007) and hyperspectral images (Mundt, et al., 2006). While data fusion is a working technique, it requires additional measurements,

calibrations, and labor relative to a single measurement. A passive hyperspectral measurement also imparts additional weather and illumination requirements for an otherwise rather environmentally insensitive LiDAR operation. Some of these problems could be avoided if the LiDAR system itself would also produce the multi- or hyperspectral information.

Traditional laser sources have restricted the LiDAR systems to using only a single or a few precise wavelengths. However, a recent development in supercontinuum lasers has made it possible to manufacture powerful fiber light sources with a continuous spectrum, that is to say, "white lasers" (Dudley, et al., 2006; Genty, et al., 2007). In supercontinuum lasers, a high peak-power laser pulse is passed through a non-linear optical fiber where the combined interaction of various non-linear optical processes transforms it into a broadband pulse. For example, a modern, micro-structured, non-linear fiber allows a 1064-nm pulse to be broadened into a spectrum ranging from 480 to 2500 nm. It is possible create a more powerful collimated beam of white light when using supercontinuum fibers lasers than it was when using traditional light sources. If such a "white laser" is combined with a hyperspectral time-of-flight sensor, then it is possible to construct an active hyperspectral LiDAR (Johnson, 1999). As technology matures, such devices can be expected to become commonly available. Currently, there is a need for virtual data to test future algorithms. Such test data can be produced using either modeling (Morsdorf, et al., 2009) or data fusion.

In publication **VI**, we presented a concept for a virtual hyperspectral LiDAR capable of producing hyperspectral 3D point clouds. According to this view, a target is measured consecutively using a commercial terrestrial laser scanner (TLS) and a custom hyperspectral scanner (HSS, Fig. 5.). The HSS exploits a supercontinuum laser source (Koheras SuperK) to actively measure backscattered reflectance

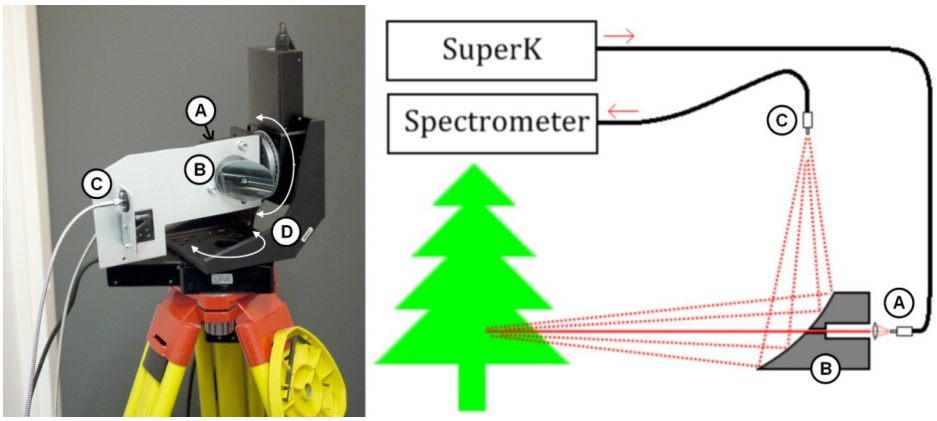

Fig. 5. On left, there is a photograph of the hyperspectral scanner (HSS) for the virtual hyperspectral LiDAR system on a tripod. On right, there is a schematic drawing (not to scale) of the operation principle for an HSS measurement. White light from the fiber of the supercontinuum laser (Koheras SuperK) (A) is collimated and the beam is guided through a hole in the centre of the receiving mirror (B). The reflected light is collected, using an off-axis paraboloid mirror, to the spectrometer optical fiber (C). The whole optical system is rotated using a turret-style, dual-axis scanner (D).

spectra. The HSS operation differs from the traditional hyperspectral measurements that use lamps or sunlight because it uses in the same backscattering measurement geometry as the laser scanners.

Since the HSS measurement produces no ranging information, the ranging data must be fused to the HSS spectra from the TLS data. The TLS provides the ranging data with a smaller footprint and a higher point density than the HSS, resulting in approximately 400 TLS points associated with each HSS spectrum. When analyzing these TLS points, it is possible to determine one or more echo distances from which the HSS spectrum is reflected. Because the HSS spectrum is a superposition of spectra from all echoes, the ranging association is well-defined only for the spectra, with a single dominating echo. The spectra with multiple echoes cannot be associated with definite ranging information. The HSS spectra with single echoes are attached to the ranging data. The attached ranging data and HSS rotator angles are used further to calculate a hyperspectral point cloud [x,y,z,R(λ)]. See publication **VI** for more technical details.

The virtual hyperspectral point clouds that were produced made it possible for us to demonstrate the capabilities of future hyperspectral LiDAR systems, including testing the hyperspectral algorithms used in point cloud classification and extracting the spectral indices used in 3D geometry.

4. Results

FIGIFIGO HDRFs and BRFs

During the research period for this dissertation (2005–2011), the FIGIFIGO was utilized in a total of 33 research campaigns or studies, producing BRFs/HDRFs of almost 400 samples now stored in the FGI Reflectance Library (see appendix A). The majority of these measurements are presented and analyzed in publications **I**–**IV**. In this chapter, the characteristics of the data type and some generalized findings from these publications are reviewed.

The quantity of data in a BRF/HDRF dataset collected using the FIGIFIGO is vast. A dataset presents the variation in a target's reflectance factor as a function of the view angle and wavelength and possibly also of the direction of illumination and linear polarization (see Figure 6.). Each of these data dimensions provides one possible way to analyze the data.

The shape of the reflectance factor spectrum is affected by the chemical composition of the target. The spectra of practically all vegetated targets have a distinct red-edge feature in the spectrum, due to the absorptions of chlorophylls, carotenoids, anthocyanidins, and a number of other pigment molecules common to all vegetation (Blackburn, 2007). Typically, vegetation reflectance factor is low (R=0.02–0.2) at visual wavelengths and rapidly increases to high values (R=0.2–0.6) after the red edge at

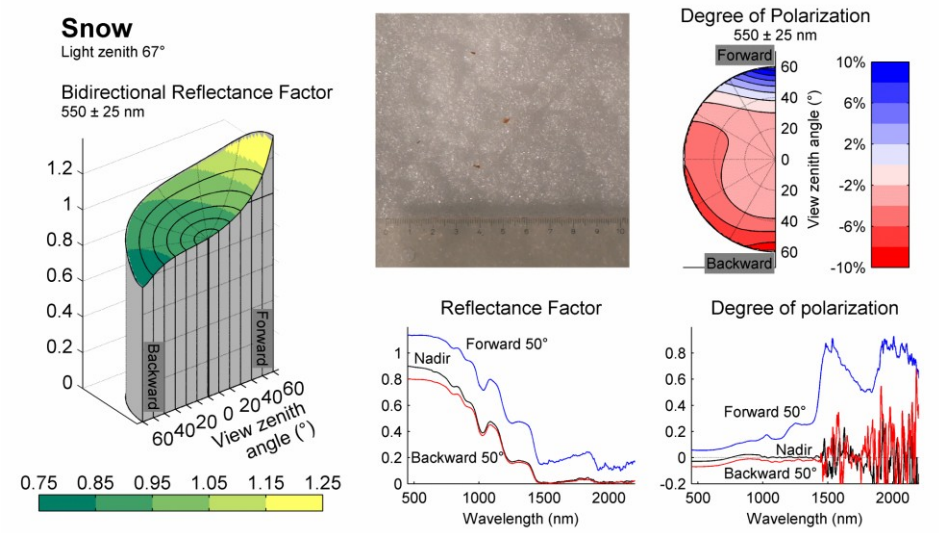

Fig. 6. A visualization of a BRF dataset for a snow sample. The image on the left shows a view angle anisotropy of the reflectance factor on a green band. The image in the middle on the top shows a photograph of the snow surface. The image in the middle on the bottom shows a reflectance factor spectrum from three view angles. The images on the right show the balance of horizontal and vertical polarization (ratio of -Q/I) as a function of the view angle (top) and wavelength (bottom).

approximately 700 nm. The spectral shapes can be used, e.g., to extract the target plant's physiology via analysis of the pigment absorptions (Blackburn, 2007; Sims and Gamon, 2002). Such generalized spectral features cannot be stated for inorganic targets, because their chemical composition varies with more freedom, but, e.g., the absorption characteristics of water can be detected from the spectra of most moist targets. Another potential spectral shape application involves determining the size of snow grains. For large snow grains, the light travels long paths inside the grains, with decreasing intensity in the strongly absorbing SWIR bands, while the intensity on visual wavelengths remains practically as high as with the small grains.

The view angle dependency of the reflectance factor has been found to correlate with the physical surface features of the targets. Targets with optically smooth surfaces (such as snow with a crust surface or asphalt) tend to scatter forward, while shadowy 3D-structured targets, such as vegetation, often tend to scatter more to backward at low viewing angles. Most of the isotropic scatterers include the reference panel material Spectralon and some gravel samples, but their reflectance is also clearly anisotropic, especially if the viewing angle is altered far away (>30°) from the nadir. Although the scattering properties are clearly linked to the structures of the samples, extraction of the exact physical properties has not seemed to provide trivial inversion schemes.

Our findings on the polarization of natural surfaces include that, in general, the land surfaces polarize weakly. The polarization is always strongest at forward angles and weakest around the nadir or 10–30° backwards from the nadir. There is also a clear spectral dependency. In general, the darker bands polarize more strongly than the brighter bands. The linear polarization in the reflectance is mostly created on first-order Fresnel reflections on the surfaces and is thus related to the surface structure of the target. However, it is not a trivial task to extract the exact physical parameters of the natural targets by exploiting linearly polarized observations and it will require modeling of the target. There are some potential signals available, e.g. in the differences between the types of snow, because the dry snow samples seem to polarize much more than the wet ones. Currently, this phenomenon remains unexplained: the simple Rayleigh or Fresnel models do not explain these observations and coherent backscattering even at best only explains it in part.

HDRFs from UAV-based mapping

In publication **V**, we presented a demonstration of HDRF mapping for a snow-covered swamp. A multi-view-angle HDRF map was produced for an area of approximately 25-by-25 meters with a 0.5 m resolution. The mapping was performed during a calm and sunny day over a target area with various types of snow. The target area consisted of a flat, frozen swamp with very few dwarf trees. A concurrent reference HDRF measurement taken with the FIGIFIGO took place just outside the bounds of the mapped area to avoid disturbing the UAV measurement. Figure 7 shows a comparison of the UAV and reference HDRFs.

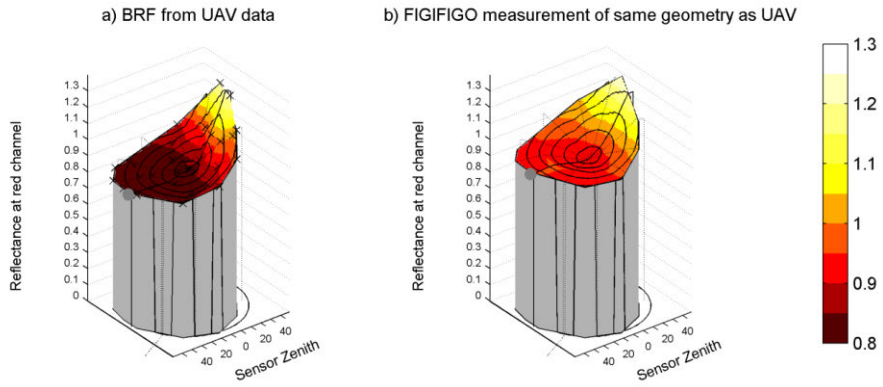

Fig. 7. The image on the left shows a reflectance factor plot for an area of smooth snow measured with the UAV. The image on the right shows a similar, but not the same, sample of smooth snow measured using the FIGIFIGO. Similar characteristics can be seen in both samples, although the overall intensity of the UAV sample is lower and the specular reflection is higher.

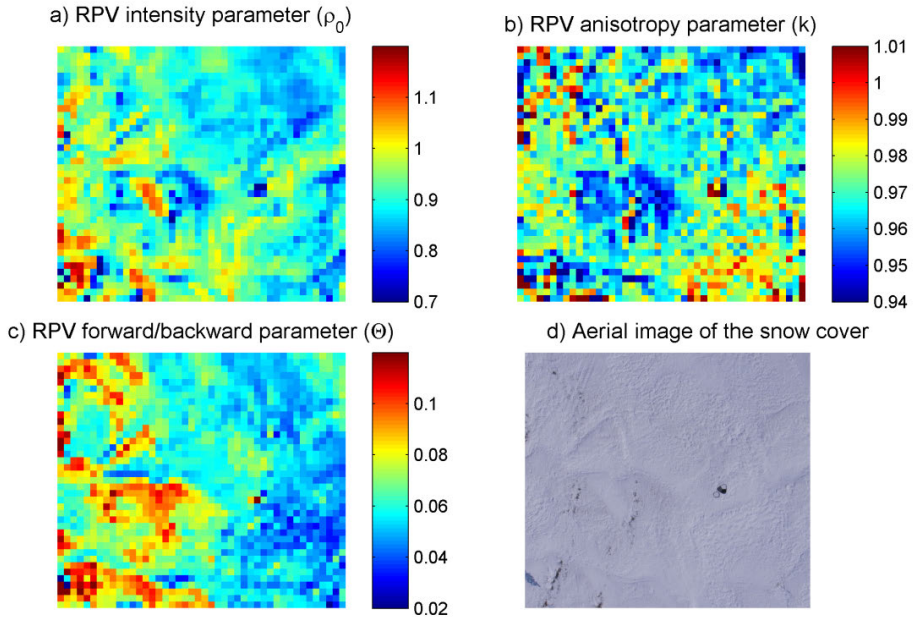

Fig. 8. Visualizations of an HDRF map of the snow covered swamp, at approximately an 0.5 m resolution. Subplots a), b), and c), depict the Rahman-Pinty-Verstraete (RPV) model parameter maps that have been fitted to the HDRF data, while subplot d) shows an unprocessed nadir photograph of the same area. The RPV model is not perfectly suited to modeling the subtle variations in the snow cover; for example, variations in the roughness of the snow cover can be observed by comparing the aerial image and the parameter maps.

Since the HDRF maps contain information in more than three dimensions, some sort of visualization is required to show them on paper. One way to do this is by fitting a BRF model to the data and visualizing the parameters of the model. A commonly used model is the Rahman-Pinty-Verstraete (RPV) model, which uses three parameters with straightforward definitions: One for describing the general intensity, a second for anisotropy, and a third one for forward/backward balance. For a more accurate definition of the parameters, see Rahman et al. (1993) or publication **V**. Figure 8 provides a visual representation of the HDRF map of the snow-covered swamp.

Virtual hyperspectral LiDAR point clouds

For publication **VI**, we measured a spruce specimen using the virtual hyperspectral LiDAR setup and produced a hyperspectral point cloud. An attempt was made to classify the point cloud between the needle, trunk, and background canvas endmember classes. The endmember spectra (Fig. 9.) were manually selected from the dataset and given a Spectral-Correlation-Mapper (SCM)classifier (de Carvalho and Meneses, 2000). The classification was expanded still further to cover the HSS spectra with multiple echoes by exploiting an advanced classifier based on a novel combination of a region-growing algorithm, an SCM algorithm, and a simulation of the reflectance spectra. Fig. 9 shows the classified point cloud of the spruce.

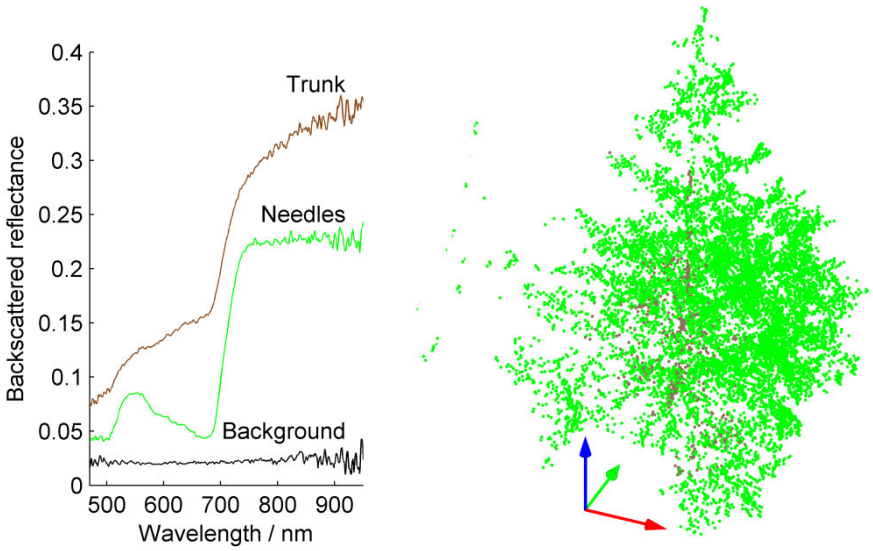

Fig. 9. The image on the left shows the backscattered reflectance spectra of the main endmember classes of the spruce sample. The image on the right shows the classified point cloud for the needle (green) and trunk (brown) endmember classes. The background points were left out of the plot.

For publication **VII**, we collected similar point clouds from a batch of young spruce, pine, and birch specimens. It was shown that a fused hyperspectral LiDAR dataset can be used for tree species' classification and that the accuracy of the classification exceeds the separate performances of both the hyperspectral and LiDAR datasets. It was also found that the spectral bands producing the best classification result for the three tree species were located at approximately 550 nm and 700 nm.

5. Discussion and outlook

Development of the FIGIFIGO

We have developed the FIGIFIGO, a novel instrument for measuring polarized BRF and HDRF in both the field and in a laboratory. Developing the FIGIFIGO has been a long iterative process, where new features have been added one by one to improve functionality and data reliability. The first version, produced in 2005, consisted only of a motorized turning arm that the spectrometer optics could be attached to. Later, the system was equipped with a number of metadata sensors, which detected, e.g., the view angle, incident irradiance, solar orientation, and GPS position. The added functional features include an active stabilization and laser pointer indication of the field-of-view position, a laboratory base with azimuth angle detection, a laboratory light system, and linearly polarizing optics. To my knowledge, the FIGIFIGO is still the only goniospectrometer capable of taking polarized measurements in field.

Each of these changes in the setup has also required changes in the storage file format and programs for data collection and processing. The first version of the FIGIFIGO measurement control program was written in Visual Basic, but as more and more features were added, the development environment was changed to LabView for improved control and clarity. The early simple data files basically contained just some metadata in the header and the user-ready reflectance factors in a tab-delimited ASCII format. With the increasing complexity of the metadata, a change in data philosophy was made and a post-processing phase was added to the data production. The output format of the control software was changed to hierarchical raw data files containing all of the sensor data with timer synchronization. Currently, the actual calculation of the BRF/HDRF dataset from the raw data is done in a Matlab environment, which provides an additional quality control phase for the data production. This processing philosophy also enables end-user files to be output in a standardized library format, independent of the minor changes to the exact measurement setup of the FIGIFIGO.

The FIGIFIGO has allowed us to collect elaborate, directional reflectance data for a number of targets, which could not have been measured using any other instrument. We have built a library of almost 400 FIGIFIGO measurements, making it one of the largest collections of multiple-view-angle reflectance datasets of documented targets in the world. These measurements have expanded our understanding of the reflectance of the natural targets; for example, based on these measurements, a review of the directional reflectance properties of various types of snow has recently been published (Peltoniemi, et al., 2010b).

The BRFs and HDRFs collected using the FIGIFIGO have been exploited in many research applications. The FIGIFIGO measurements that have had the most direct impact on practical remote sensing are probably those used to produce reflectance-factor, ground-reference data for space and airborne imaging. An example of this has been presented in publication **V**. In addition, the FIGIFIGO has been exploited when taking HDRF and BRF measurements of the FGI Sjökulla radiometric test field gravels (Honkavaara, et al., 2008; Honkavaara, et al., 2010) and the FGI reflectance reference tarpaulins (Markelin, et al., 2008). These targets have been further used for the vicarious calibration/validation of aerial photography cameras (Honkavaara, et al., 2011; Markelin, et al., 2010). In another series of studies, the HDRFs of large, uniform open areas, such as sports fields, asphalt

areas, and beach sand, were measured in the Helsinki Metropolitan Area. These data were exploited for evaluation atmospheric correction methods involving SPOT satellite images (Clark, et al., 2010; Clark, et al., 2011a; Clark, et al., 2011b). The FIGIFIGO has also been exploited for the SNORTEX measurement campaign (Roujean, et al. 2009).

The FIGIFIGO data have also been used in a number of environmental studies. Surface hemispherical albedo is a quantity indicating the amount of incident radiation to a surface that is reflected away from the surface and it is an essential variable in climate change studies. FIGIFIGO data have been used for calculating hemispherical albedos for selected targets and for evaluating the broadband albedo conversion formulae used in satellite applications (Peltoniemi, et al., 2010a). In another study, the forest understory vegetation and land-cover spectra collected with the FIGIFIGO were used to examine the influence of understory vegetation on forest reflectance in the Arctic region (Rautiainen, et al., 2007).

Development of UAV-based HDRF mapping

We have developed the first system to acquire multiple-view-angle HDRF maps exploiting a micro UAV and a consumer camera. It was also shown that even the small consumer cameras can be used for retrieving accurate reflectance factors when a reflectance reference target is present in every image. The current concept, as presented in publication **IV**, can be used to acquire local HDRF maps, e.g. for providing calibration/validation reference data for aerial or high-resolution satellite sensors or for generalizing the FIGIFIGO HDRF measurements to a larger sampling.

Although radio-controlled helicopters and airplanes have already been available for decades, the technology for autonomous UAVs is currently developing rapidly. The late development in autonomous or semi-autonomous flight modes has made it possible to successfully perform remote sensing tasks even without years of piloting experience. Despite their apparent ease of use, the UAVs are still rather unstable platforms and thus minor and major crash landings are certain to occur every once in a while. Also, the payload weight, maximum flight time, stability of the flight, accuracy of inertia and positioning systems, and weather and wind restrictions on the current small helicopter UAVs still make it necessary to improve UAVs. The HDRF mapping in publication **IV** was done using a small quadrocopter UAV with a payload of only 200g. Such a payload can only house the smallest pocket cameras. The current larger helicopter and fixed-wing UAVs can carry payloads exceeding 1 kg. Such a payload can already house more professional single-lens reflex cameras or even custom camera systems built around an industrial camera.

A major drawback to the HDRF mapping setup presented here is the requirement that every image have a reference target because this restricts the spatial expansion of the mapping task. The reference target is always needed because of the high variability in the quality of the photos taken by the pocket cameras. Such small cameras are generally not designed to emphasize radiometric quality, because this is not required for consumer-grade pictures. The aforementioned advanced cameras are potentially designed with better radiometric control, allowing better exposure stability between images. Having access to such a stable camera for an HDRF mapping application would make it possible to calibrate all of the reflectance factor images using the reference target only on one or two images. Such an improvement would make it possible to map larger areas and further bridge the scale gap between ground reference and traditional airborne measurements.

Development of the virtual hyperspectral LiDAR

We have developed a prototype of a virtual hyperspectral LiDAR and demonstrated its performance for tree species classification. The system is one of the first scanning systems that measures the hyperspectral reflectance in direct backscattering geometry and probably the very first that exploits a supercontinuum laser source. The setup works well as a method for producing fused, hyperspectral point clouds, but the concept still has some major flaws when it comes to the practical applications. Fusing the data between a hyperspectral scanner and a separate ranging instrument causes extra labor and calibration issues both in terms of measurements and point cloud generation. The regular unamplified spectrometer is not an ideal sensor for detection, because it significantly limits the range and speed of the measurement. Also, the intensity stability of the supercontinuum laser and the durability of the fiber were found to be less than desirable. Eye-safety issues were found to be troublesome for taking measurements outside the laboratory. Although some minor flaws were found with the laser source, the most important conclusion from these studies was the fact that the supercontinuum lasers were shown to be a feasible technology that could be used in future hyperspectral LiDARs.

The findings on the virtual hyperspectral LiDAR have encouraged us to continue working to develop hyperspectral LiDARs, i.e. integrated systems that collect both the reflected spectrum and the ranging information in one shot. First, a two-color-channel LiDAR was constructed using the supercontinuum laser and two avalanche photodiodes (Chen, et al., 2010). Recently, the work was continued by constructing a true scanning hyperspectral LiDAR with up to 16 color channels (Hakala, et al., 2012). Such spectral information makes it possible to exploit the hyperspectral classification and data extraction techniques, including calculating various spectral indices and classifying them according to their spectral correlation. Our recent experiences with the technical feasibility of acquiring and potentially utilizing hyperspectral LiDAR data have been encouraging. Thus, I believe that in the near future the significance of such instruments in remote sensing is certain to increase rapidly.

Outlook

With the wide library of FIGIFIGO and UAV data on natural surfaces, it is possible to draw some conclusions about potential improvements that could be made to some remote sensing practices and concepts.

- In most remote sensing applications, the view-angle effects in reflectance factors are ignored and treated as an error. Our results show that the view-angle effects are strongest on the solar principal plane, while the reflectance is more isotropic in the cross-plane direction. This remark allows for the possibility of optimizing aerial-imaging flight lines. If the anisotropic effects are to be minimized, the flight lines should be oriented directly towards and away from the Sun. This practice eliminates the usage of pixels in highly anisotropic backward and forward scattering geometries, because the subsequent images usually overlap with one another in the direction of the flight line.
- Many spectrometers, cameras, and calibration systems have spurious polarization sensitivity, especially at extreme angles or wavelengths. Thus, it may be necessary to consider polarization even for the basic non-polarizing instruments. Our studies have showed that, in general, the natural targets polarize weakly in the nadir direction, but that the degree of polarization increases at the forward angles. Thus, for typical airborne or satellite imaging or

for spectrometry taken close to the nadir, the polarization effects can usually be safely ignored. On the other hand, care should be taken to minimize the polarization sensitivity of sensors observing targets in the forward geometry.

- As mentioned above, the polarization is strongest in forward scattering where the reflectance is dominated by the horizontally polarized light. This polarization at the forward angles is usually accompanied by a brightening, which causes high anisotropy in the reflectance factor intensity. In some imaging or spectrometric applications, if one can afford to lose half of the intensity, a single linear polarizer could be used to reduce the anisotropic reflectance effect. Prior to attaching the polarizer, one should make sure that the possible polarization sensitivity of the sensor does not cause problems.
- The polarization spectra of natural targets tend to reproduce the characteristic shapes of the unpolarized reflectance factor spectra. Thus, a polarization spectrometry could be a useful instrument in cases where normal reflectance spectrometry fails, e.g. because they lack a reference or because the illumination varies too much, since the polarization measurements do not need any hard-to-estimate normalizer. The typical polarization spectra seem to have quite smooth wavelength dependencies that are predictable at short ranges. Thus, for practical purposes, a low spectral resolution will suffice.

All three of the instruments presented in this dissertation have proven to be useful research tools for demonstrating novel measurement techniques and providing novel reflectance data for the targets. The instruments have pioneered the use of a number of novel technical innovations that can be exploited to improve the accuracy and ease of use of the future measurement setups. The library for FGI HDRF and BRF data is currently being transported to an online database open to all researchers (the link to the database can be found at *www.fgi.fi* and *www.specchio.ch*).

References

Auriol, F., Leon, J.-F., Balois, J.-Y., Verwaerde, C., Francois, P., Riedi, J., Parol, F., Waquet, F., Tanré, D., Goloub, P., 2008. Multidirectional visible and shortwave infrared polarimeter for atmospheric aerosol and cloud observation: OSIRIS (Observing System Including PolaRisation in the Solar Infrared Spectrum), Larar, A.M., Lynch, M.J. and Suzuki, M. (Eds.), SPIE, December 5, 2008, pp. 71491D.

Barnsley, M.J., Settle, J.J., Cutter, M.A., Lobb, D.R., Teston, F., 2004. The PROBA/CHRIS mission: a low-cost smallsat for hyperspectral multiangle observations of the Earth surface and atmosphere. IEEE Transactions on Geoscience and Remote Sensing 42 (7), 1512.

Biliouris, D., Verstraeten, W.W., Dutré, P., van Aardt, J.A., Muys, B., Coppin, P., 2007. A Compact Laboratory Spectro-Goniometer (CLabSpeG) to Assess the BRDF of Materials. Presentation, Calibration and Implementation on Fagus sylvatica L. Leaves. Sensors 7 (9), 1846-1870.

Blackburn, G.A., 2007. Hyperspectral remote sensing of plant pigments. Journal of experimental botany 58 (4), 855-867.

Bourgeois, C.S., Ohmura, A., Schroff, K., Frei, H., Calanca, P., 2006. IAC ETH Goniospectrometer: A Tool for Hyperspectral HDRF Measurements. Journal of Atmospheric and Oceanic Technology 23 (4), 573-584.

Brissaud, O., Schmitt, B., Bonnefoy, N., Douté, S., Rabou, P., Grundy, W., et al., 2004. Spectrogonio Radiometer for the Study of the Bidirectional Reflectance and Polarization Functions of Planetary Surfaces. 1. Design and Tests. Applied Optics 43 (9), 1926-1937.

Browell, E.V., Ismail, S., Grant, W.B., 1998. Differential absorption lidar (DIAL) measurements from air and space. Applied Physics B: Lasers and Optics 67 (4), 399-410.

Chen, Y., Räikkönen, E., Kaasalainen, S., Suomalainen, J., Hakala, T., Hyyppä, J., et al., 2010. Two-channel Hyperspectral LiDAR with a Supercontinuum Laser Source. Sensors 10 (7), 7057-7066.

Clark, B., Suomalainen, J., Pellikka, P., 2011a. An historical empirical line method for the retrieval of surface reflectance factor from multi-temporal SPOT HRV, HRVIR and HRG multispectral satellite imagery. International Journal of Applied Earth Observation and Geoinformation 13 (2), 292-307.

Clark, B., Suomalainen, J., Pellikka, P., 2011b. The selection of appropriate spectrally bright pseudo-invariant ground targets for use in empirical line calibration of SPOT satellite imagery. ISPRS Journal of Photogrammetry and Remote Sensing 66 (4), 429-445.

Clark, B., Suomalainen, J., Pellikka, P., 2010. A comparison of methods for the retrieval of surface reflectance factor from multitemporal SPOT HRV, HRVIR, and HRG multispectral satellite imagery. Canadian Journal of Remote Sensing 36 (4), 397-411.

Coburn, C.A., Peddle, D.R., 2006. A low-cost field and laboratory goniometer system for estimating hyperspectral bidirectional reflectance. Canadian Journal of Remote Sensing 32 (3), 244-253.

de Carvalho, O.A., Meneses, P.R., 2000. Spectral Correlation Mapper (SCM): An Improvement on the Spectral Angle Mapper (SAM), Pasadena, CA, USA ed. In: NASA JPL AVIRIS Workshop, 23-25 February, 65-74.

Dudley, J.M., Genty, G., Coen, S., 2006. Supercontinuum generation in photonic crystal fiber. Reviews of Modern Physics 78 (4), 1135-1184.

Ehrlich, A., Bierwirth, E., Wendisch, M., Herber, A., Gayet, J.-F., 2011. Airborne hyperspectral surface and cloud bi-directional reflectivity observations in the Arctic using a commercial, digital camera. Atmos. Chem. Phys. Discuss. 11 24591–24629.

Feret, J., François, C., Asner, G.P., Gitelson, A.A., Martin, R.E., Bidel, L.P.R., Ustin, S.L., le Maire, G., Jacquemoud, S., 2008. PROSPECT-4 and 5: Advances in the leaf optical properties model separating photosynthetic pigments. Remote Sensing of Environment 112 (6), 3030-3043.

Gatebe, C.K., King, M.D., Platnick, S., Arnold, G.T., Vermote, E.F., Schmid, B., 2003. Airborne spectral measurements of surface–atmosphere anisotropy for several surfaces and ecosystems over southern Africa. Journal of Geophysical Research 118 (D13), 8489-8504.

Genty, G., Coen, S., Dudley, J., 2007. Fiber supercontinuum sources. Journal of the Optical Society of America B 24 (8), 1771-1785.

Giardino, C., Brivio, P.A., 2003. The application of a dedicated device to acquire bidirectional reflectance factors over natural surfaces. International Journal of Remote Sensing 24 (14), 2989-2995.

Hagolle, O., Goloub, P., Deschamps, P.-Y., Cosnefroy, H., Briottet, X., Bailleul, T., Nicolas, J.-M., Parol, F., Lafrance, B., Herman, M., 1999. Results of POLDER in-flight calibration. Geoscience and Remote Sensing, IEEE Transactions on 37 (3), 1550-1566.

Hakala, T., Suomalainen, J., Kaasalainen, S., Chen, Y., 2012. Full waveform hyperspectral LiDAR for terrestial laser scanning. Optics Express 20 (7), 7119-7127

Hapke, B., 1993. Theory of Reflectance and Emittance Spectroscopy, Cambridge University Press,.

Honkavaara, E., Peltoniemi, J.I., Ahokas, E., Kuittinen, R., Hyyppä, J., Jaakkola, J., Kaartinen, H., Markelin, L., Nurminen, K., Suomalainen, J., 2008. A permanent test field for digital photogrammetric systems. Photogrammetric Engineering & Remote Sensing. 74 (1), 95-106

Honkavaara, E., Hakala, T., Peltoniemi, J., Suomalainen, J., Ahokas, E., Markelin, L., 2010. Analysis of Properties of Reflectance Reference Targets for Permanent Radiometric Test Sites of High Resolution Airborne Imaging Systems. Remote Sensing 2 (8), 1892-1917.

Honkavaara, E., Nurminen, K., Markelin, L., Suomalainen, J., Ilves, R., 2011. Calibrating and validating multispectral 3D imaging systems at a permanent test site – case study with an Intergraph DMC. The Photogrammetric Record 26 (134), 229-249.

Hyyppä, J., Wagner, W., Hollaus, M., Hyyppä, H., 2009. Airborne Laser Scanning, In: The SAGE Handbook of remote sensing, Warner, T.A., Nellis, M.D. and Foody, G.M. (Eds.), SAGE Publications, 199-210.

Irish, J.L., Lillycrop, W.J., 1999. Scanning laser mapping of the coastal zone: the SHOALS system. ISPRS Journal of Photogrammetry and Remote Sensing 54 (2-3), 123-129.

Jacquemoud, S., Verhoef, W., Baret, F., Bacour, C., Zarco-Tejada, P.J., Asner, G.P., et al., 2009. PROSPECT+SAIL models: A review of use for vegetation characterization. Remote Sensing of Environment 113, Supplement 1 (0), S56-S66.

Johnson, B., 1999. Compact active hyperspectral imaging system for the detection of concealed targets, In: Detection and Remediation Technologies for Mines and Mine-like targets IV, Orlando Florida, April 1999, Proceedings of SPIE 3710, 144-153.

Koechler, C., Hosgood, B., Andreoli, G., Schmuck, G., Verdebout, J., Pegoraro, A., et al., 1994. The European optical goniometric facility: technical description and first experiments on spectral unmixing, In: IEEE International Geoscience and Remote Sensing Symposium, Pasadena, 1994. Proc. of IGARSS'94, 4, 2375-2377.

Kokhanovsky, A.A., Aoki, T., Hachikubo, A., Hori, M., Zege, E.P., 2005. Reflective properties of natural snow: approximate asymptotic theory versus in situ measurements. Geoscience and Remote Sensing, IEEE Transactions on 43 (7), 1529-1535.

Kovalick, W.M., Graham, D.W., Bur, M.J.C., 1994. Data processing and calibration of the Advanced Solid-State Array Spectroradiometer In: IEEE International Geoscience and Remote Sensing Symposium, Pasadena, 1994. Proc. of IGARSS'94, 3, 1652-1654.

Leblanc, S.G., Bicheron, P., Chen, J.M., Leroy, M., Cihlar, J., 1999. Investigation of directional reflectance in boreal forests with an improved four-scale model and airborne POLDER data. , IEEE Transactions on Geoscience and Remote Sensing 37 (3), 1396-1414.

Leroux, C., Deuzé, J.-L., Coulomb, P., Sergent, C., Fily, M., 1998. Ground measurements of the polarized bidirectional reflectance of snow in the near-infrared spectral domain: Comparison with model results. Journal of Geophysical Research 103, 18721-18731.

Li, S., Zhou, X., 2004. Modelling and measuring the spectral bidirectional reflectance factor of snow-covered sea ice: an intercomparison study. Hydrological Processes 18 (18), 3559-3581.

Lichti, D., Pfeifer, N., Maas, H., 2008. ISPRS Journal of Photogrammetry and Remote Sensing theme issue "Terrestrial Laser Scanning". ISPRS Journal of Photogrammetry and Remote Sensing 63 (1), 1-3.

Lucht, W., Lewis, P., 2000. Theoretical noise sensitivity of BRDF and albedo retrieval from the EOS-MODIS and MISR sensors with respect to angular sampling. International Journal of Remote Sensing 21 (1), 81-98.

Markelin, L., Ahokas, E., Honkavaara, E., Peltoniemi, J.I., Kukko, A., Hyyppä, J., Kuittinen, R., 2008. Portable reflectance targets and their use in radiometric evaluation and calibration of digital photogrammetric cameras. Photogrammetric Engineering & Remote Sensing. 74 (12), 1487-1500.

Markelin, L., Honkavaara, E., Hakala, T., Suomalainen, J., Peltoniemi, J., 2010. Radiometric stability assessment of an airborne photogrammetric sensor in a test field. ISPRS Journal of Photogrammetry and Remote Sensing 65 (4), 409-421.

Meister, G., Wiemker, R., Bienlein, J., Spitzer, H., 1996. In situ BRDF measurements of selected surface materials to improve analysis of remotely sensed multispectral imagery. International archieves for photogrammetry and remote sensing XXXI 493-498.

Milton, E.J., Schaepman, M.E., Anderson, K., Kneubühler, M., Fox, N., 2009. Progress in field spectroscopy. Remote Sensing of Environment 113, Supplement 1 (0), S92-S109.

Morsdorf, F., Nichol, C., Malthus, T., Woodhouse, I.H., 2009. Assessing forest structural and physiological information content of multi-spectral LiDAR waveforms by radiative transfer modelling. Remote Sensing of Environment 113 (10), 2152-2163.

Mundt, J.T., Streuker, D.R., Glenn, N.F., 2006. Mapping Sagebrush Distribution Using Fusion of Hyperspectral and Lidar Classifications. Photogrammetric Engineering & Remote Sensing 72 (1), 47-54.

Painter, T.H., Paden, B., Dozier, J., 2003. Automated spectro-goniometer: A spherical robot for the field measurement of the directional reflectance of snow. Review of Scientific Instruments 74 (12), 5179-5188.

Pegrum, H., Fox, N., Chapman, M., Milton, E., 2006. Design and Testing a New Instrument to Measure the Angular Reflectance of Terrestrial Surfaces, In: IEEE International Geoscience and Remote Sensing Symposium, Denver, 2006. Proc. of IGARSS 2006, 1119-1122.

Peltoniemi, J.I., Kaasalainen, S., Näränen, J., Rautiainen, M., Stenberg, P., Smolander, H., et al., 2005. BRDF measurement of understory vegetation in pine forests: dwarf shrubs, lichen and moss. Remote Sensing of Environment 94 (3), 343-354.

Peltoniemi, J.I., Manninen, T., Suomalainen, J., Hakala, T., Puttonen, E., Riihelä, A., 2010a. Land Surface Albedos Computed from BRF Measurements with a Study of Conversion Formulae. Remote Sensing 2 (8), 1918-1940.

Peltoniemi, J.I., Suomalainen, J., Hakala, T., Näränen, J., Puttonen, E., Kaasalainen, S., et al., 2010b. Reflectance of various snow types: measurements, modeling, and potential for snow melt monitoring, In: Light Scattering Reviews 5, Kokhanovsky, A.A. (Ed.), Springer, 291-347.

Pust, N.J., Dahlberg, A.R., Thomas, M.J., Shaw, J.A., 2011. Comparison of full-sky polarization and radiance observations to radiative transfer simulations which employ AERONET products. Optics Express 19 (19), 18602-18613.

Rahman, H., Pinty, B., Verstraete, M.M., 1993. Coupled Surface-Atmosphere Reflectance (CSAR) Model 2. Semiempirical Surface Model Usable With NOAA Advanced Very High Resolution Radiometer Data. 98 20791-20801.

Rautiainen, M., Suomalainen, J., Mõttus, M., Stenberg, P., Voipio, P., Peltoniemi, J.I., et al., 2007. Coupling forest canopy and understory reflectance in the arctic latitudes of Finland. Remote Sensing of Environment 110, 332-343.

Roujean, J., Manninen, T., Kontu, A., Peltoniemi, J., Hautecoeur, O., Riihelä, A., et al., 2009. SNORTEX (Snow Reflectance Transition Experiment): Remote Sensing Measurement of the Dynamic Properties of the Boreal Snow-forest in Support to Climate and Weather Forecast: Report of IOP-2008. In: IEEE International Geoscience and Remote Sensing Symposium, Cape Town, 2009. Proc. of IGARSS'2009, 2, 859-862.

Schaaf, C.B., Gao, F., Strahler, A.H., Lucht, W., Li, X., Tsang, T., et al., 2002. First operational BRDF, albedo nadir reflectance products from MODIS. Remote Sensing of Environment 83 (1–2), 135-148.

Schaepman-Strub, G., Schaepman, M., Painter, T.H., Dangel, S., Martonchik, J.V., 2006. Reflectance Quantities in Optical Remote Sensing - Definitions and Case Studies. Remote Sensing of Environment 103 (1), 27-42.

Schopfer, J., Dangel, S., Kneubühler, M., Itten, K.I., 2008. The Improved Dual-view Field Goniometer System FIGOS. Sensors 8, 5120-5140.

Secord, J., Zakhor, A., 2007. Tree Detection in Urban Regions Using Aerial Lidar and Image Data. IEEE Geoscience and Remote Sensing Letters 4 (2), 196-200.

Sims, D.A., Gamon, J.A., 2002. Relationships between leaf pigment content and spectral reflectance across a wide range of species, leaf structures and developmental stages. Remote Sensing of Environment 81 (2–3), 337-354.

Sparks, W.B., Hough, J.H., Kolokolova, L., Germer, T.A., Chen, F., DasSarma, S., DasSarma, P., Robb, F.T., Manset, N., Reid, I.N., Macchetto, F.D., Martin, W., 2009 Circular polarization in scattered light as a possible biomarker. Journal of Quantitative Spectroscopy and Radiative Transfer 110 (14–16), 1771-1779.

Strangi, G., Ferjani, S., Barna, V., De Luca, A., Versace, C., Scaramuzza, N., et al., 2006. Random lasing and weak localization of light indye-doped nematic liquid crystals. Optics Express 14 (17), 7737-7744.

Sun, Z., Zhao, Y., 2011. The effects of grain size on bidirectional polarized reflectance factor measurements of snow. Journal of Quantitative Spectroscopy and Radiative Transfer 112 (14), 2372-2383.

Taixia, W., Yunsheng, Z., 2005. The bidirectional polarized reflectance model of soil. IEEE Transactions on Geoscience and Remote Sensing 43 (12),.2854-2859.

Turner, M., 1998. The Sandmeier Field Goniometer: A measurement tool for bi--directional reflectance, John C. Stennis Space Center, MS ed. In: NASA Commercial Remote Sensing Verification and Validation Symposium 1998, pp. 1-6.

Tyo, J.S., Goldstein, D.H., Chenault, d.B., Shaw, J.A., 2006. Review of passive imaging polarimetry for remote sensing applications. Applied Optics 45 (22), 5453-5469.

Verstraete, M.M., Gobron, N., Aussedat, O., Robustelli, M., Pinty, B., Widlowski, J., et al., 2008. An automatic procedure to identify key vegetation phenology events using the JRC-FAPAR products. Advances in Space Research 41 (11), 1773-1783.

Widlowski, J., Taberner, M., Pinty, B., Bruniquel-Pinel, V., Disney, M.I., Fernandes, R., et al., 2006. The third RAdiation transfer Model Intercomparison (RAMI) exercise: Documenting progress in canopy reflectance modelling. Journal of Geophysical Research 112 (D09111),.

Wiersma, D.S., Bartolini, P., Lagendijk, A., Righini, R., 1997. Localization of light in a disordered medium. Nature 390 (6661), 671-673.

Yang, F., Kumar, A., Wang, W., Juang, H.H., Kanamitsu, M., 2001. Snow Albedo Feedback and Seasonal Climate Variability over North America. Journal of Climate 14 (22), 4245-4248.

Appendix A: FIGIFIGO campaigns and targets 2005–2011

Campaign: **2005SodankylaSnowNorsen**
'2005-04-17-snow_morning'
'2005-04-17_snow_afternoon'
'2005-04-18_snow_with_lamp'
'2005-04-19-night-snow'
'2005-04-19_snow'
'2005-04-20_snow_in_the_swamp'
'2005-04-21_snowswamp'
'2005-04-22_night_snow'
'2005-04-23_snow'

Campaign: **2005Suonenjoki**
'2005-06-07_J1_Jakala1 cleaned'
'2005-06-07_R1_Risuja1'
'2005-06-07_S1_Sammal1 cleaned'
'2005-06-07_S1_Sammal1 natural'
'2005-06-08_LL1_Lingon+lichen natural'
'2005-06-08_M1_Mustikka1'
'2005-06-09_J2_palleroporonjakala'
'2005-06-09_K1_karike'
'2005-06-09_LL1-
Cut_Lichen_without_lingon'
'2005-06-09_LM2-cut_lingon+moss_cut'
'2005-06-09_LM2_lingon+moss'
'2005-06-09_M1-
Cut_Mustikka1_alussammal'

Campaign: **2005Vegetation**
'2005-06-20_blueberry'
'2005-06-20_undersoil'
'2006-07-19_Football_field'

Campaign: **2006NorsenSummer2**
'2006-08-20_Cottongrass_Andoya'
'2006-08-22_lingon_with_crowberry'
'2006-08-22_lingon_with_crowberry2'
'2006-08-24_dwarfbirch'
'2006-08-24_dwarfbirch2'
'2006-08-24_dwarfbirch3'
'2006-08-24_dwarfbirch4'

Campaign: **2006Sodankyla**
'2006-08 Yhteismittaus maston kanssa'
'2006-08-03_Crowberry'
'2006-08-03_Heather'
'2006-08-03_Lichen'
'2006-08-03_lichen2'
'2006-08-05_crowberry2'
'2006-08-05_heather2'
'2006-08-05_heather3'
'2006-08-05_lichen3'
'2006-08-05_lingonberry'
'2006-08-05_soil'
'2006-08-06_lichen4'
'2006-08-06_lingonberry2(moss_crowberry)'
'2006-08-06_lingonberry3(lichen)'
'2006-08-06_sand'
'2006-08-08_Light_Gray_Sand'
'2006-08-08_Sand'
'2006-08-08_soil2'

Campaign: **2007Snow**
'2007-04-17_Snow1'
'2007-04-18_Polarization_test'
'2007-04-18_Snow2'
'2007-04-20_Snow_Polarisation'

Campaign: **2007SodankylaUnderstorey**
'2007-07-02 Heather1'
'2007-07-02 Needles & Sand'
'2007-07-03 CrowberryA1'
'2007-07-03 Heather & Crowberry'
'2007-07-03 Lichen & Needles'
'2007-07-03 Lingonberry1'
'2007-07-04 CrowberryB2'
'2007-07-04 Lichen1'
'2007-07-04 Lichen2'
'2007-07-04 Lichen3'
'2007-07-04 Lichen4'
'2007-07-04 Lichen5'
'2007-07-05 CrowberryC1'
'2007-07-05 Heather3'
'2007-07-05 Heather5'
'2007-07-05 Heather6'
'2007-07-05 Heather7'

Campaign: **2008ReflectanceTarps**
'2008-10-14 Tarp20'
'2008-10-21 Tarp05'
'2008-10-21 Tarp25'
'2008-10-21 Tarp30'
'2008-10-21 Tarp50'

Campaign: **2008SjokullaGravels**
'2008-07-01 Gray Gravel'
'2008-07-02 White Gravel Non-polarized'
'2008-07-02 White Gravel Polarized'
'2008-08-06 White Gravel Field'
'2008-09-11 Sjokulla Black Gravel'
'2008-09-11 Sjokulla Gray Gravel'
'2008-09-12 SjokullaOldBlackGravel'
'2008-10-28 Lab B1 Black Gravel'
'2008-10-28 Lab B1 Black Gravel Polarized'
'2008-10-28 Lab B2a Black Gravel'
'2008-10-28 Lab B2a Black Gravel
Polarized'
'2008-10-28 Lab B2b Black Gravel'
'2008-10-28 Lab B2b Black Gravel
Polarized'
'2008-10-28 Lab G2 Gray Gravel'
'2008-10-28 Lab G2 Gray Gravel Polarized'
'2008-10-28 Lab R1 Red Gravel'
'2008-10-28 Lab R1 Red Gravel Polarized'
'2008-10-28 Lab W2 White Gravel'
'2008-10-28 Lab W2 White Gravel Polarized'

Campaign: **2008SodankylaSnow**
'2008-04-01 Old snow with lamp'
'2008-04-02 Old snow with lamp 2'
'2008-04-03 Old snow in plain in sunlight'
'2008-04-04 New snow with lamp'
'2008-04-05 New snow with lamp 2'

Campaign: **2008TarpCanditates**
'2008-03-25 blackpaint1layer'
'2008-03-25 fabricPlasticWebbing'
'2008-03-25 graycarpet_backside'
'2008-03-25 graycarpet_frontside'
'2008-03-25 whitepaint1layer'
'2008-03-26 blackrubbermatt_backside'
'2008-03-26 darkgraycarpet_frontside'
'2008-03-26 lightgraycarpet_backside'
'2008-03-26 lightgraycarpet_frontside'
'2008-03-26 thickwhitefabric'
'2008-03-26 whitethinfabric_x2'
'2008-03-26 whitethinfabric_x4'
Campaign: **2008UlrichBeislTarps**
'2008-10-21 BlueTarp'
'2008-10-21 LargeGrayPaintedTarp'
'2008-10-21 LargePaintedUnderside'
'2008-10-21 SilverTarp'
'2008-10-21 WhiteTarp'

Campaign: **2009AsteroidSurfaces**
'2009-01-20 Oman Sand 1'
'2009-02-26 Lunar Regolith Simualnt Rough'
'2009-02-26 Lunar Regolith Simulant Dense'
'2009-02-26 Lunar Regolith Simulant Loose'

Campaign: **2009Hyytiala**
'2009-05-31 HyytialaAsphalt'
'2009-05-31 HyytialaBeachvolley'
'2009-05-31 HyytialaGrass'
'2009-05-31 HyytialaGravel'

Campaign: **2009MasalaSnow**
'2009-03-19 Snow Masala Field'
'2009-03-19 Snow Masala Field2'
'2009-03-20 Snow FGI Lab'

Campaign: **2009PaintedTarpSamples**
'2009-05-25 GrayTarp'
'2009-08-05 BlackTarp'
'2009-08-05 GrayTarp'

Campaign: **2009PaintedTiles**
'2009-03-10 BlueOneLayerTVT_L358'
'2009-03-10 BrickGrayTVT_4991'
'2009-03-10 BrickUnpainted'
'2009-03-10 BrickWhiteTVT_6500'
'2009-03-10 GrayOneLayerTVT_4991'
'2009-03-10 GrayTwoLayerTVT_4991'
'2009-03-10 GreenOneLayerTVT_L380'
'2009-03-10 RedThreeLayerTVT_M320'
'2009-03-10 UnpaintedRedTile'
'2009-03-10 UnpaintedThickTile'
'2009-03-10 UnpaintedThinTile'
'2009-03-10 UnpaintedWhiteGravel'
'2009-03-10 WhiteThinOneLayerTVT_4986'
'2009-03-10 WhiteTwoLayer4986'
'2009-03-10 WhiteTwoLayer6500'
'2009-03-10 YellowTwoLayerTVT_K302'
'2009-08-03 BlueTile1'
'2009-08-03 BlueTile2'
'2009-08-03 GrayBrick'
'2009-08-03 GreenTile'
'2009-08-03 RedTile'
'2009-08-03 ThickGray1'
'2009-08-03 ThickGray2'
'2009-08-03 ThickWhite1'
'2009-08-03 ThickWhite2'
'2009-08-03 ThinGrayTile'
'2009-08-03 ThinWhiteTile'
'2009-08-03 UnpaintedRed'
'2009-08-03 UnpaintedThickTile'
'2009-08-03 UnpaintedThinTile'
'2009-08-03 WhiteBrick'
'2009-08-03 WhiteGravelTile'
'2009-08-03 YellowTile'
'2009-09-25 BlueTile1'
'2009-09-25 BlueTile2'
'2009-09-25 BrickGray'
'2009-09-25 BrickWhite'
'2009-09-25 GreenTile'
'2009-09-25 RedTile'
'2009-09-25 ThickGray1'
'2009-09-25 ThickGray2'
'2009-09-25 ThickWhite1'
'2009-09-25 ThickWhite2'
'2009-09-25 ThinGray'
'2009-09-25 ThinWhite'
'2009-09-25 UnpaintedRed'
'2009-09-25 UnpaintedThick'
'2009-09-25 UnpaintedThin'
'2009-09-25 WhiteGravelTile'
'2009-09-25 YellowTile'

Campaign: **2009PolarizedVegetation**
'2009-09-24 Grass'
'2009-09-24 Grassb'
'2009-10-08 Lichen'
'2009-10-09 Lichen'
'2009-10-13 Lichen'
'2009-10-13 Lichen4'

Campaign: **2009SjokullaGravels**
'2009-05-05 B1'
'2009-05-05 B2a'
'2009-05-05 B2b'
'2009-05-05 G2'
'2009-05-05 R1'
'2009-05-05 W2'
'2009-06-25 Black Gravel'
'2009-06-25 GrayGravel'
'2009-06-25 WhiteGravel'
'2009-08-03 B1'
'2009-08-03 B2a'
'2009-08-03 B2b'
'2009-08-03 G2'
'2009-08-03 R1'
'2009-08-03 W2'
'2009-09-25 B1'
'2009-09-25 B2a'
'2009-09-25 B2b'
'2009-09-25 G2'
'2009-09-25 R1'
'2009-09-25 W2'

Campaign: **2009Snortex**
'2009-04-20 Kommattivaara 1'
'2009-04-21 NorsenMastLamp1'
'2009-04-22 MantovaaranaapaRoughSnow1'
'2009-04-22 MantovaaranaapaRoughSnow2'
'2009-04-22 MantovaaranaapaRoughSnow3'
'2009-04-22
MantovaaranaapaSmoothSnow1'
'2009-04-23 KorppiaapaIce1'
'2009-04-23 KorppiaapaRoughSnow1'

Campaign: **2009UAVReferenceTargets**
'2009-04-07 Gray Cardboard'
'2009-04-07 Gray Fabric'
'2009-04-07 Square Gray'
'2009-04-07 Square White'
'2009-04-07 Triange White'
'2009-04-07 Triangle Black'
'2009-04-07 Triangle Gray'
'2009-08-03 ArtificialGrass'
'2009-08-19 PTFE'
'2009-08-19 SquareWhite'

Campaign: **2010EerosLaserReference**
'2010-11-09 A1_1'
'2010-11-09 A1_10'
'2010-11-09 A1_2'
'2010-11-09 A1_3'
'2010-11-09 A1_4'
'2010-11-09 A1_5'
'2010-11-09 A1_6'
'2010-11-09 A1_7'
'2010-11-09 A1_8'
'2010-11-09 A1_9'

Campaign: **2010Greenland**
'2010-06-29 Snow1'
'2010-06-30 Snow1'
'2010-06-30 Snow2'
'2010-06-30 Snow3'
'2010-07-01 Snow1'
'2010-07-01 Snow2'
'2010-07-01 Snow3'
'2010-07-01 Snow4'
'2010-07-04 Snow1'
'2010-07-04 Snow2'
'2010-07-05 Snow1'
'2010-07-05 Snow2'
'2010-07-05 Snow3'
'2010-07-05 Snow4'
'2010-07-05 Snow5'
'2010-07-07 Snow1'
'2010-07-07 Snow2'
'2010-07-07 Snow3'
'2010-07-07 Snow4'
'2010-07-07 Snow5'
'2010-07-07 Snow6'
'2010-07-07 Snow7'
'2010-07-08 Snow1'
'2010-07-08 Snow2'
'2010-07-08 Snow3'
'2010-07-08 Snow4'
'2010-07-09 Snow1a'
'2010-07-09 Snow1b'
'2010-07-09 Snow1c'
'2010-07-09 Snow1d'
'2010-07-10 Snow1e'
'2010-07-11 Snow1Diffuse'
'2010-07-11 Snow2Diffuse'
'2010-07-12 Snow1'
'2010-07-12 Snow10Pol'
'2010-07-12 Snow2'
'2010-07-12 Snow3'
'2010-07-12 Snow4'
'2010-07-12 Snow5'
'2010-07-12 Snow6'
'2010-07-12 Snow7'
'2010-07-12 Snow8'
'2010-07-12 Snow9'
'2010-07-13 Snow1Pol'
'2010-07-13 Snow2Pol'
'2010-07-13 Snow3Pol'
'2010-07-13 Snow4'
'2010-07-13 Snow5'

Campaign: **2010PaintedTiles**
'2010-05-12 BlueTile1'
'2010-05-12 BlueTile2'
'2010-05-12 BrickGray'
'2010-05-12 BrickWhite'
'2010-05-12 GreenTile'
'2010-05-12 RedTile'
'2010-05-12 ThickGray1'
'2010-05-12 ThickGray2'
'2010-05-12 ThickWhite1'
'2010-05-12 ThickWhite2'
'2010-05-12 ThinGray'
'2010-05-12 ThinWhite'
'2010-05-12 UnpaintedRed'
'2010-05-12 UnpaintedThick'
'2010-05-12 UnpaintedThin'
'2010-05-12 WhiteGravelTile'
'2010-05-12 YellowTile'
'2010-05-18 BlueTile2'
'2010-05-18 GreenTile'
'2010-05-18 RedTile'
'2010-05-18 ThickGray1'
'2010-05-18 ThickWhite1'
'2010-05-18 ThinGray'
'2010-05-18 ThinWhite'
'2010-05-18 YellowTile'
'2010-09-03 BlueTile1'
'2010-09-03 BlueTile2'
'2010-09-03 BrickGray'
'2010-09-03 BrickWhite'
'2010-09-03 GreenTile'
'2010-09-03 RedTile'
'2010-09-03 ThickGray1'
'2010-09-03 ThickGray2'
'2010-09-03 ThickWhite1'
'2010-09-03 ThickWhite2'
'2010-09-03 Thin Gray'
'2010-09-03 ThinWhite'
'2010-09-03 UnpaintedRed'
'2010-09-03 UnpaintedThick'
'2010-09-03 UnpaintedThin'
'2010-09-03 WhiteGravelTile'
'2010-09-03 YellowTile'

Campaign: **2010PolarizedLabTargets**
'2010-05-07 PolarizedSand'
'2010-05-27 PolarizedSand'
'2010-05-28 PolarizedSand'
'2010-05-31 BlackTarp'

Campaign: **2010ReferenceReflectanceTarps**
'2010-09-06 Tarp05'
'2010-09-06 Tarp20'
'2010-09-06 Tarp25'
'2010-09-06 Tarp30'
'2010-09-06 Tarp50'

Campaign: **2010SjokullaGravels**
'2010-05-12 B1'
'2010-05-12 B2a'
'2010-05-12 B2b'
'2010-05-12 G2'
'2010-05-12 R1'
'2010-05-12 W2'
'2010-09-06 B2a'
'2010-09-06 B2b'
'2010-09-06 W2'
'2010-09-08 B1'
'2010-09-08 G2'
'2010-09-08 R1'

Campaign: **2010Snortex**
'2010-03-16 Snow1'
'2010-03-16 Snow2'
'2010-03-17 Snow3'
'2010-03-18 Snow4'
'2010-03-18 Snow5'
'2010-03-21 Snow6'
'2010-03-21 Snow7'
'2010-03-21 Snow8'
'2010-03-21 Snow9'
'2010-03-22 Snow10'
'2010-03-22 Snow11'
'2010-03-22 Snow12'
'2010-03-22 Snow13'

Campaign: **2010UAVReference**
'2010-05-18 SquareGray'
'2010-05-18 SquareWhite'
'2010-05-19 TriangleBlack'
'2010-05-19 TriangleGray'
'2010-05-19 TriangleWhite'

Campaign: **2011PaintedTiles**
'2011-06-14 RedTile'
'2011-06-14 ThickWhite1'
'2011-06-14 ThinGray'
'2011-06-14 ThinWhite'
'2011-06-15 BlueTile1'
'2011-06-15 BlueTile2'
'2011-06-15 BrickGray'
'2011-06-15 BrickWhite'
'2011-06-15 GreenTile'
'2011-06-15 ThickGray1'
'2011-06-15 ThickGray2'
'2011-06-15 ThickWhite2'
'2011-06-15 UnpaintedRed'
'2011-06-15 UnpaintedThick'
'2011-06-15 UnpaintedThin'
'2011-06-15 WhiteGravelTile'
'2011-06-15 YellowTile'

Campaign: **2011SjokullaAISA**
'2011-07-20 B2South'
'2011-07-20 G2'
'2011-07-20 Tarp20'
'2011-07-20 Tarp30'
'2011-07-20 W2'

Campaign: **2011SjokullaGravels**
'2011-06-21 B1'
'2011-06-21 B2a'
'2011-06-21 B2b'
'2011-06-21 G2'
'2011-06-21 R1'
'2011-06-21 W2'